Analogue models of lithospheric-scale rifting monitored in an X-ray CT scanner

Frank Zwaan[1] and Guido Schreurs[2]

[1]Helmholtz Centre Potsdam - GFZ German Research Centre for Geosciences
[2]University of Bern

November 24, 2022

Abstract

Rifting and continental break-up are fundamental tectonic processes, the understanding of which is of prime importance. However, the vast temporal and spatial scales involved pose major limitations to researchers. Analogue tectonic modelling represents a great means to mitigate these limitations, but studying internal deformation in lithospheric-scale models remains a challenge. We therefore present a novel method for lithospheric-scale rifting models that are uniquely monitored in an X-ray CT-scanner. CT-scanning, combined with digital image correlation (DIC) techniques, provides unparalleled insights into model deformation. Our models show that the degree of coupling between competent lithospheric layers, which are separated by a weak lower crustal layer, strongly impacts rift system development. Low coupling isolates the upper crust from the upper lithospheric mantle layer below, preventing an efficient transfer of deformation between both layers. By contrast, fast rifting increases coupling, so that deformation in the mantle is efficiently transferred to the upper crust, inducing either a symmetric or asymmetric (double) rift system. The observation that asymmetric deformation can initiate during the earliest rifting stages challenges the two-phase scenario involving initial symmetric rifting, prior to subsequent asymmetric rifting. Oblique divergence leads to en echelon graben arrangements, and seemingly delays break-up, somewhat in contradiction to concepts of oblique divergence promoting break-up. These insights provide an incentive to further run lithsospheric-scale rifting models, and to apply advanced monitoring techniques to extract as much information as possible from these. There is indeed a broad range of opportunities for follow-up studies within and beyond the field of rift tectonics.

Analogue models of lithospheric-scale rifting monitored in an X-ray CT scanner

F. Zwaan[1,2], and G. Schreurs[1]

[1]University of Bern, Institute of Geological Sciences, Bern, Switzerland

[2]Helmholtz Centre Potsdam - GFZ German Research Centre for Geosciences, Potsdam, Germany

Corresponding author: Frank Zwaan (frank.zwaan@geo.unibe.ch)

Key Points:

- We present the first-ever analogue models of lithospheric-scale rifting monitored in an X-ray CT scanner, revealing their internal evolution
- The degree of coupling between competent lithospheric layers controls the transfer of deformation between them, and thus the rift style
- Some results contradict previous studies, and the successful application of our new method provides a strong incentive for follow-up work

Abstract

Rifting and continental break-up are fundamental tectonic processes, the understanding of which is of prime importance. However, the vast temporal and spatial scales involved pose major limitations to researchers. Analogue tectonic modelling represents a great means to mitigate these limitations, but studying internal deformation in lithospheric-scale models remains a challenge. We therefore present a novel method for lithospheric-scale rifting models that are uniquely monitored in an X-ray CT-scanner. CT-scanning, combined with digital image correlation (DIC) techniques, provides unparalleled insights into model deformation. Our models show that the degree of coupling between competent lithospheric layers, which are separated by a weak lower crustal layer, strongly impacts rift system development. Low coupling isolates the upper crust from the upper lithospheric mantle layer below, preventing an efficient transfer of deformation between both layers. By contrast, fast rifting increases coupling, so that deformation in the mantle is efficiently transferred to the upper crust, inducing either a symmetric or asymmetric (double) rift system. The observation that asymmetric deformation can initiate during the earliest rifting stages challenges the two-phase scenario involving initial symmetric rifting, prior to subsequent asymmetric rifting. Oblique divergence leads to en echelon graben arrangements, and seemingly delays break-up, somewhat in contradiction to concepts of oblique divergence promoting break-up. These insights provide an incentive to further run lithsospheric-scale rifting models, and to apply advanced monitoring techniques to extract as much information as possible from these. There is indeed a broad range of opportunities for follow-up studies within and beyond the field of rift tectonics.

Plain Language Summary

The Earth's surface consitst of tectonic plates that are in constant motion, driven by titanic forces deep within the planet. One of the key plate teconic processes is the stretching (rifting) and eventual break-up of continents and the opening of oceanic basins. Understanding the mechanisms involved is of great importance. However, studying continental break-up is challenging due to the vast size of the plate tectonic systems, and the extensive timescales over which they unfold; plate tectonic processes can rarely be directly observed. A practical solution to this issue is the use of analogue experiments, which reproduce these processes in a matter of hours or days in a modestly sized laboratory. However, a major obstacle that remains is the opacity of these models: similar to tectonic plates, these models are opaque, so that their internal evolution remains hidden. X-Ray CT-scanning provides a unique means to reveal a model's internal structures during a model run. Here we present the first-ever application of CT-scanning to monitor relatively complex lithospheric-scale models of continental rifting. The CT-scans provide unique insights into the internal evolution of such models, some of which are in contradiction with previous works, and various possibilities for follow-up studies exist.

1 Introduction

Rifting and the formation of rifted margins during continental break-up represent a fundamental part of the Wilson cycle (e.g. Wilson 1966; Wilson et al. 2019), and a thorough understanding of the dynamic evolution of rifts and rifted margins, and the processes involved is of prime importance for various reasons. Not only do rifts and rifted margins harbour for vast fossil energy reserves (Levell et al., 2010; Zou et al., 2015), they also have great potential for geothermal energy production (e.g. Freymark et al. 2017; Burnside et al. 2020; Bonechi et al. 2021) and potentially natural hydrogen production (Smith et al. 2005), and their sedimentary archives yield crucial insights into past global and climate change (Haq et al., 1987; Catuneanu et al., 2009; Kirschner et al., 2010; Catuneanu and Zecchin, 2013). However, these areas where large parts of the global human population are concentrated are also at risk from e.g. volcanism, earthquakes, (submarine) landslides and tsunamis (Gouin 1979; Brune, 2016; Biggs et al. 2021). Hence a thorough understanding of the geological processes that shape rifts and rifted margin is of utmost importance to human society.

However, geologists face various challenges when studying the evolution of rifts and rifted margins. Firstly, these tectonic systems extend over vast areas so that studying them in detail is highly challenging. Furthermore, direct access to rift and rifted margins is often very limited since large parts of these systems are situated below sea level, and on top of that, are often covered by thick post-rift sedimentary sequences. These challenges have been somewhat overcome through the use of geophysical techniques, especially seismic methods and the drilling of deep boreholes. However, possibly the most significant and lasting obstacle on our way to understanding rift processes is caused by the long timescales at which they occur, as it is simply not possible to directly observe the development of rift systems over millions of years.

In order to overcome this major obstacle, geologist have since long applied scaled analogue models, which allow the simulation of systems and processes at vast spatial and temporal scales within a matter of hours or days in a modest laboratory, using relatively simple analogue materials at limited financial costs. A large number of analogue modelling studies focusing on rift tectonics have been published, and these studies have yielded a wealth of useful insights, as summarized in various reviews and overview papers (Vendeville et al. 1987; McClay 1990, 1996; Allemand & Brun 1991; Beslier 1991; Naylor et al. 1994; Koyi 1997; Brun 1999, 2002; Michon & Merle 2000, 2003; Corti et al. 2003; Bahroudi et al. 2003; Corti 2012; Brun et al. 2018, Zwaan et al. (2019; 2021a, 2021b) and Zwaan & Schreurs (in press).

Of these analogue modelling studies, a large part focuses on crustal-scale structures, which is permissible when considering small-scale processes or very early-stage rift stages, but these relatively simple models cannot capture the full rift system. Especially important when considering the full scope of continental break-up is the influence of the asthenosphere, i.e. the isostatic compensation that asthenospheric flow exerts on a rift system. In analogue modelling studies that simulate lithospheric-scale rifting in a normal gravity field, the isostatic influence of the asthenosphere is generally simulated with a dense low-viscosity fluid (syrup or honey), on which the model materials representing the lithosphere float (e.g. Allemand & Brun 1991; Benes & Davy 1996; Benes & Scott 1996; Brun & Beslier 1996; Sun et al. 2009; Capelletti et al. 2013; Autin et al. 2010, 2013; Nestola et al. 2013, 2015; Molnar et al. 2017, 2018; Beniest et al. 2018;

Samsu et al. 2021, Fig. 1). The rheological layering of lithospheric-scale models in an enhanced gravity field (i.e. centrifuge models) is very similar, although the materials are generally of a higher viscosity in such experiments (e.g. Corti 2008; Agostini et al. 2009; Corti et al. 2013).

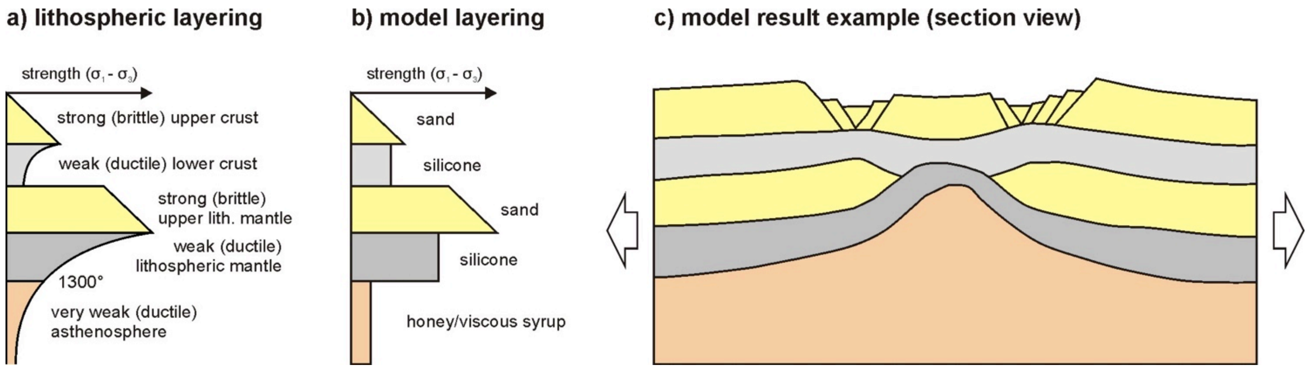

Fig. 1. *Example of lithospheric-scale rifting model set-up and result. (a) Strength profile of a 4-layer lithosphere in nature. (b) Analoge model materials used to reproduce the natural strength profile in panel (a). (c) Example of a 4-layer model result obtained at the end of a model run. Adopted from Zwaan et al. (2019), based on Allemand & Brun (1991).*

However, all of these previous lithospheric-scale rifting models have an important disadvantage in that the internal model evolution has so far not been monitored and analysed in real time. Where the internal deformation of crustal-scale models can in some cases be partly observed via a glass sidewall (while accounting for boundary friction effects), the internal deformation of lithosphere-scale models remains elusive since the model lithosphere generally contains different (sticky viscous) layers that hamper direct observation of the model interior through glass. These viscous layers also hamper the use of surface structures and topography (including the topography of the base of the lithosphere, e.g. Nestola et al. 2013, 2015) as reliable indicators for internal deformation since these layers often decouple internal model deformation from the surface structures (e.g. Allemand et al. 1989; Molnar et al. 2017; 2018; Zwaan et al. 2019; 2021a, 2021b, Fig. 1). Sectioning is another option to gain insight into a model's interior, but this is a destructive method that can only be used to interpret the model evolution through the reconstruction of markers, and only after completion of the model (e.g. Beslier 1991; Brun & Beslier 1996). Furthermore, sectioning of lithospheric-scale models containing various viscous layers is often a challenging task since the models are highly unstable and deform easily while making the sections. The same goes for removing the crustal layers to scan the topography of the base of the MOHO after the model run (Nestola et al. 2015).

So far the only reliable non-destructive method to truly peek into otherwise opaque analogue models materials during an experimental run is X-Ray CT-scanning (e.g. Colletta et al. 1991; Schreurs et al. 2003). This technique, which basically relies on density differences within the model materials (e.g. induced by layering and dilatation along faults) has been around for a number of decades and has been applied in various studies to analyse crustal-scale rifting models, (e.g. Zwaan et al. 2016; 2018; 2020; Schmid et al. 2021). Yet to our knowledge CT-scanning has so far never been used to analyse the much more complex deformation in lithospheric-scale models, providing a strong incentive to push forward the state of the art in modelling.

The aim of this paper is therefore to present the unique possibilities of a newly designed analogue model set-up for studying lithospheric-scale rifting, which allows for the first time the monitoring of model-internal deformation via X-Ray CT scanning methods. The resulting CT imagery does not only allow a qualitative assessment of internal model evolution, but we can even quantify strain within the model through the use of digital image correlation (DIC) techniques normally applied for strain analysis of model surfaces. Furthermore, next to simple orthogonal rifting our new set-up enables us to simultaneously simulate lateral movements as well, opening many possibilities for simulating different tectonic regimes such as oblique extension and (oblique) basin inversion. In this paper we present the results from a total of four rifting models that not only demonstrate the general viability and potential of this new modelling procedure, but also have implications for the interpretation of natural rift systems during orthogonal and oblique rifting.

2 Methods

2.1 Materials

Similar to previous analogue modelling studies of lithospheric-scale rifting (e.g. Allemand & Brun 1991; Brun & Beslier 1996; Nestola et al. 2015, Fig. 1), we apply both brittle and viscous materials to simulate the brittle and ductile parts of the lithosphere, as well as the asthenosphere (Fig. 2c). Assuming a stable 4-layer continental lithosphere prior to deformation, the model consists from top to bottom of a strong (brittle) upper crust (UC), a (weak) ductile lower crust (LC), a strong (brittle) upper lithospheric mantle (ULM), a weak (ductile) lower lithospheric mantle (LLM) and a very weak (ductile) asthenosphere with the following relative layer thickness: 2:1:1.5:2 (Fig. 2c, Tables 1, 2).

Table 1. Brittle material properties

Granular materials	**Feldspar sand**[a]	**Liaver beads**[b]
Represents	**UC and ULM**	**-**
Grain size range (ø)	100-250 µm	100-300 µm
Density (sieved) (ρ_{sieved})	ca. 1300 kg/m^3	ca. 530 kg/m^3
Internal peak friction angle (φ_p)	35.0°	36.0°
Dynamic-stable friction angle (φ_d)	29.9°	28.6°
Reactivation friction angle (φ_r)	32.0°	30.1°
Cohesion (C)	51 Pa	0 Pa

[a] Feldspar sand properties after Zwaan et al. (2022a)
[b] Liaver beads properties after Warsitzka et al. (2019)

Table 2. Viscous material properties

Viscous materials	**Pure PDMS**[a]	**Viscous mixture 1**[b]	**Viscous mixture 2**[b]	**Glucose syrup**[c]
Represents	**-**	**Lower crust**[d]	**Lower Lith. Mantle**[d]	**Asthenosphere**
Weight ratio PDMS : corundum sand	-	1 : 0.52	1: 0.7	-
Density (ρ)	965 kg/m^3	ca. 1300 kg/m^3	ca. 1400 kg/m^3	ca. 1450 kg/m^3
Viscosity[e] (η)	ca. $2.8 \cdot 10^4$ Pa·s	ca. $6 \cdot 10^4$ Pa·s	ca. $8 \cdot 10^4$ Pa·s	ca. 65 Pa·s
Rheology[f]	Newtonian (n = 1)	near-Newtonian (n = 1.05-1.10)	near-Newtonian (n = 1.05-1.10)	near-Newtonian (n = ca. 1.09)

[a] Pure PDMS rheology after Rudolf et al. (2016) and Zwaan et al. (2018)
[b] Rheology of viscous mixtures 1 and 2 after Zwaan et al. (2018)
[c] Glucose syrup rheology after Schmid et al. (2022b)
[d] Viscosity value holds for model strain rates < 10^{-4} s^{-1}
[e] Power-law exponent n (dimensionless) represents sensitivity to strain rate

For both the brittle upper crust and brittle upper mantle layer, we use FS900S feldspar sand produced by Amberger Kaolinwerke (https://www.quarzwerke.com) (Table 1). This angular feldspar sand as provided by the company has a main grain size between 100-250 μm (65% or grains, see grain size distribution in Willingshofer et al. 2018). In contrast to other modelling studies (e.g. Beniest et al. 2018), we do not have the means to sieve and remove the fine fraction of this FS900S sand to the 100-250 μm range prior to use. However, new ring shear tests at GFZ Potsdam show that not removing the finer fraction of the feldspar sand does not significantly affect the internal friction angle (Zwaan et al. 2022a). The density of the feldspar sand is ca. 1300 kg/m^3 when added into the model by means of sieving from a height of ca. 30 cm.

The ductile lower crust and ductile lower lithospheric mantle are simulated using viscous mixtures of SGM-36 silicon oil (Polydimethylsiloxane or PDMS) formerly produced by Dow Corning, now part of Dow Chemical (www.dow.com), and F120 corundum sand acquired from Carlo AG (www.carloag.ch) (Table 2). The PDMS has a bulk density of 965 kg/m^3 (Rudolf et al. 2016), whereas the corundum in the corundum sand has a bulk density of 3950 kg/m^3. The grain size of the corundum sand is between 88 and 125 μm. By mixing these components in different ratios, we obtain viscous materials with different (near-Newtonian) rheology and varying densities. We use a mixture with a density of ca. 1300 kg/m^3 and a viscosity of 6×10^4 Pa·s (viscous mixture 1) to simulate the lower crust, while a mixture with a density of ca. 1400 kg/m^3 and a 8×10^4 Pa·s (viscous mixture 2) for the lower lithospheric mantle (Zwaan et al. 2018, Table 2).

These four layers representing the lithosphere float on top of a Glucosweet 44 glucose syrup layer simulating the asthenosphere (Fig. 2c, Table 2). This glucose syrup is acquired from ADEA (https://www.adea-srl.it/) and has a density of ca. 1450 kg/m^3. The higher density of the syrup with respect to the overlying model materials prevents the latter materials from sinking into the syrup. Rheometer test performed at University of Roma TRE show that the syrup has a near-Newtonian rheology with a relatively low viscosity of ca. 65 Pa·s, when compared to the viscosity of 8×10^4 Pa·s of the lowermost viscous layer (Zwaan et al. 2018; Schmid et al. 2022b, Table 2). This viscosity difference is similar to the viscosity difference between the lithosphere and asthenosphere in nature (Figs. 1, 2c).

In order to mark layering (both within sand layers, as well as between brittle and viscous layers) on CT imagery (section 2.4), we add thin layers (≤ 1 mm) of "Liaver beads", i.e. foamed glass beads produced by Liaver (www.liaver.com), (grain size between 100 and 300 μm, density = ca. 530 kg/m^3, Warsitzka et al. 2019). The Liaver beads have very different X-ray attenuation coefficients with respect to the other analogue model materials and clearly stand out on CT images. Since the Liaver beads have similar internal friction angles as the feldspar sand (Table 1), and are only used as thin layers within brittle model materials or to mark the transition between the syrup and the lower viscous layer, their use is not considered to have any major impact on model deformation.

2.2. Set-up

The general modelling set-up principle is similar to previous analogue models of lithospheric-scale rifting with a lithosphere floating on a heavy fluid, with the exception that our set-up specifically allows for oblique rifting and X-Ray CT-scanning (Figs. 1, 2, section 2.). The current set-up is based on a conceptual design by Zwaan (2017) and has been constructed by engineers from IPEK, Ostschweizer Fachhochschule in Rapperswil. It includes a number of components that are added to the highly versatile NAMAZU machine, also developed by IPEK, which has been used for various previous analogue modelling studies at the Tectonic Modelling Laboratory of the Institute of Geological Sciences at the University of Bern (e.g. Klinkmüller 2011; Alonso-Henar et al. 2015; Zwaan et al. 2016; 2018; 2020; 2021a, b; Fedorik et al. 2019; Schori et al. 2021).

Our new set-up includes a large basin containing the glucose syrup and is installed on the NAMAZU machine. A rectangular framework of inner sidewalls that contain the materials representing the model lithosphere is hung down in this basin (Fig. 2a, c). These inner sidewalls are fixed to bars that on their turn are connected to computer-controlled motors. Motors Y1 and Y2 can induce orthogonal extension of the model materials contained within the inner framework, or, in combination with simple-shear motion (imposed by motor X1), can produce oblique rifting (Fig. 2d-f). The direction of oblique rifting is defined as the angle α, which is the angle between the model to the long model axis and the combined directions of the motors (Fig. 1f). Importantly, as the model is deforming, the syrup can freely flow below the inner model sidewalls, allowing for isostatic compensation at the base of the simulated lithosphere that analogue models with a fixed base lack (e.g. Zwaan et al. 2019). The short inner sidewalls are equipped with hinges and consist of overlapping plates to accommodate the (oblique) rifting applied in the models, while still containing the model materials representing the lithosphere within the inner framework (Fig. 1a, f). Importantly, the experimental set-up is constructed from X-Ray transparent materials that allow for optimal X-Ray CT-scanning.

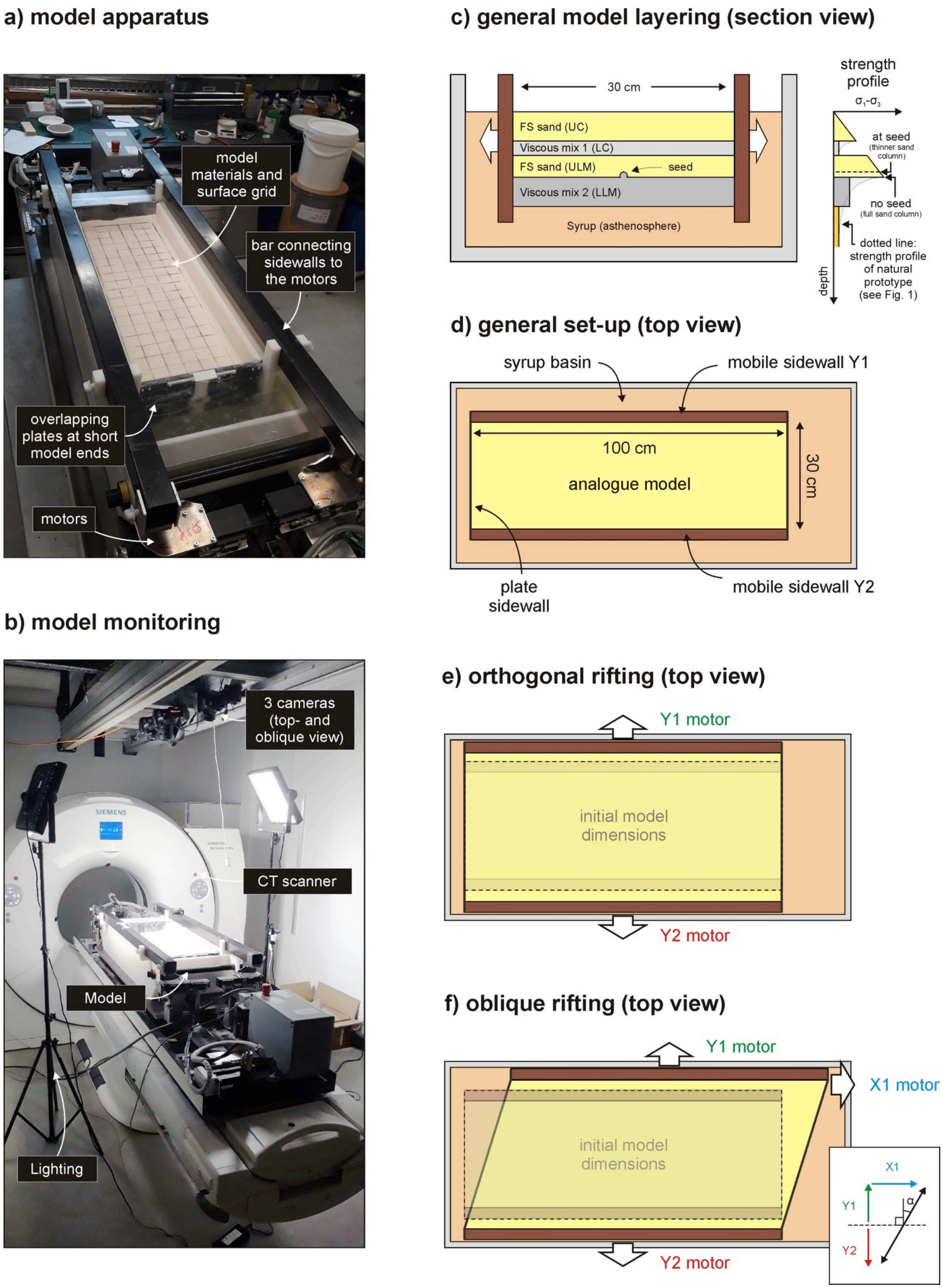
a) model apparatus
model materials and surface grid
bar connecting sidewalls to the motors
overlapping plates at short model ends
motors
b) model monitoring
3 cameras (top- and oblique view)
CT scanner
Model
Lighting
c) general model layering (section view)
30 cm
FS sand (UC)
Viscous mix 1 (LC)
FS sand (ULM)
seed
Viscous mix 2 (LLM)
Syrup (asthenosphere)
strength profile
σ1-σ3
at seed
(thinner sand column)
no seed
(full sand column)
dotted line: strength profile of natural prototype (see Fig. 1)
depth
d) general set-up (top view)
syrup basin
mobile sidewall Y1
100 cm
analogue model
30 cm
plate sidewall
mobile sidewall Y2
e) orthogonal rifting (top view)
Y1 motor
initial model dimensions
Y2 motor
f) oblique rifting (top view)
Y1 motor
X1 motor
initial model dimensions
Y2 motor
X1
Y1
α
Y2

Fig. 2. Model set-up. (a) Model apparatus with the different components of the set-up and its link to the NAMAZU machine. (b) Model run in the CT-scanning with the camera rig, lighting and the CT scanner itself. The model runs in 15 min intervals, after which it is halted and moved into the CT-scanner to obtain CT slices perpendicular to the long axis of the model. (c) Schematic cross-section of the model set-up depicting the model layering and the space for the syrup to move below the inner sidewalls for isostatic compensation. FS: feldspar sand, LC: lower crust, LLC: lower lithospheric mantle. UC: upper crust, ULM: upper lithospheric mantle. On the right: a schematic strength profile of the model layering and its natural equivalent (compare with Fig. 1). (d) Schematic top view of the model set-up. (e-f) Schematic top view of model deformation and the motors involved: (e) orthogonal rifting, and (f) oblique rifting.

2.3. Model preparation and parameters

Preparing the models involves a number of steps including freezing of the syrup to stabilize the model materials during model construction. All steps are described in detail in the supplementary material (i.e. a data publication by Zwaan & Schreurs 2022b). The details of the four models completed for this study are provided below and in Table 3.

Model A serves as a reference model. It involves orthogonal rifting and the total lithospheric thickness is half that of the subsequent models (i.e. the thicknesses of the UC, LC, ULM and LLM were 10 mm, 5 mm, 7.5 mm and 10 mm, respectively). The model does not contain any structural inheritance to localize deformation and under the standard divergence velocity (10 mm/h). The total model duration amounts to 150 min for a total of 25 mm of divergence, and the model is CT-scanned.

Model B and C also involve orthogonal rifting at the same standard divergence velocity as Model A, but have a standard model thickness of 20 mm, 10 mm, 15 mm and 20 mm for the UC, LC, ULM and LLM, respectively. Another contrast to Model A is the insertion of a weakness or “seed”, a rod of viscous material at the base of the brittle ULM layer, to localize deformation. Such seeds have been used in various previous modelling studies to simulate linear weaknesses such as crustal shear zones (e.g. Le Calvez & Vendeville 2002; Zwaan et al. 2016, 2021a, 2021b; Osagiede et al. 2021; Schmid et al. 2022a), but we apply them in the modelled upper lithospheric mantle instead (Fig. 1c). Furthermore, these models undergo a total of 50 mm of divergence over a 5-hour period. Model C is a rerun of Model B in the CT scanner.

Finally Model D involves the same standard layering as Models B and C, but initially undergoes 45˚ oblique rifting at the standard divergence velocity of 10 mm/h for the first 195 min (32.5 mm of divergence). Subsequently, the divergence velocity is tripled to 10 mm/h for the remaining 105 min of the model run, covering an additional 52.5 mm of divergence, so that the total extension amounts to 85 mm.

Table 3: *Model parameters*

Model	Seed		Divergence direction (angle α)*	Divergence velocity (Y1 + Y2)[#]	Divergence velocity (X1)[#]	Effective divergence velocity	Model Duration	Total displacement (at angle α)	CT-scanned
A[¥]	No		0˚	10 mm/h	0 mm/h	10 mm/h	150 min	25 mm	Yes
B[$]	Yes		0˚	10 mm/h	0 mm/h	10 mm/h	240 min	40 mm	-
C	Yes		0˚	10 mm/h	0 mm/h	10 mm/h	300 min	50 mm	Yes
D[§]	Yes	Phase 1:	45˚	7.2 mm/h	7.2 mm/h	10 mm/h	195 min	32.5 mm	Yes
		Phase 2:	45˚	21.6 mm/h	21.6 mm/h	30 mm/h	105 min	52.5 mm	Yes

* See definition of angle α in Fig. 2f
\# See definition of Y1, Y2 and X1 in Fig, 2d-f
¥ Half layer thickness (see text)
$ Technical issues: parts of time-lapse imagery missing (break between t = 75 min and t = 180 min)
§ Total model duration: 300 min; total divergence: 85 mm

2.4. Scaling

Applying analogue modeling scaling laws (e.g. Hubbert 1937; Ramberg 1981; Weijermars & Schmeling 1986) demonstrates the suitability of our models for simulating continental rifting processes (detailed scaling calculations can be found in Appendix A1). Specifically, the (standard) models have a geometric scaling ratio of $6.7\cdot10^{-7}$, so that 1 cm corresponds to 15 km in nature, and the 6.5 thick lithospheric layering represents a ca. 100 km thick lithosphere in nature. The standard divergence velocity in our Models B, C and D (10 mm/h) translates to ca. 3.2 mm/yr in nature, whereas the faster velocity in the second phase of Model D (30 mm/h) translates to 9.6 mm/yr in nature. The 10 mm/h divergence in Model A, which has a thinner simulated lithosphere, amounts to 11 mm/yr. These values are close to plate divergence velocities observed in natural rift systems (e.g. the East African Rift, Saria et al. 2014), and also dimensionless scaling ratios are very similar between model and nature, demonstrating that scaling requirements are fulfilled (Appendix A2).

2.5. Model monitoring and analysis

We use various techniques to monitor and analyse our models and the deformation they undergo during the four model runs. Firstly, we use a rig containing three high-resolution D810 Nikon cameras, one of which provides top view images, and the other two inclined (stereoscopic) images of the model surface (Fig 1b). These cameras are programmed via a computer to take pictures every 30 sec, creating time-lapse series. At the same time, we apply a timer for the lighting on one side of the model to switch on and off every 30 sec, so that we obtain a time series of images with and without shade (each with 1 minute intervals).

The images with shade provide visual clues about surface deformation, whereas the images without shade are ideal for 2D (map view) strain analysis. This strain analysis is done using digital image correlation (DIC) DaVis 10.1 software from LaVision (www.lavision.de), which compares surface patterns on images (if needed after correction for their inclination) from different time steps and detects deformation. The result is a detailed and quantified analysis of surface model deformation over time.

Furthermore, the inclined images, preferably without shade, allow for stereoscopic reconstruction of the model topography over time through Agisoft Photoscan photogrammetry software (www.agisoft.com). By comparing the different distortions of the images from the stereoscopic images, the software can reconstruct the 3D model surface for selected time steps. These 3D surfaces are georeferenced using reference markers with known locations placed on the model set-up, to produce properly georeferenced digital elevation models (DEMs). These DEMs are subsequently post-processed in QGIS (www.qgis.org), an open source geographic information system (GIS) software.

Next to 3D photography and the quantitative surface analyses it enables, the key innovation in terms of model monitoring and analysis in our study is the application of X-ray CT-scanning techniques (e.g. Sassi et al. 1993; Colletta et al. 1991, Schreurs et al. 2003; Holland et al. 2011; Zwaan et al. 2018; Schmid et al. 2022a), allowing us to for the first time trace the internal 3D structural evolution of this type of models. The X-Ray CT-scanning of Models A, C and D is done in the 64 slice Siemens Somatom Definition AS apparatus at the Institute of Forensic Medicine of the University of Bern. For practical reasons, the central 50 cm area is selected for CT-scanning in each of the scanned models. Scanning intervals are 15 min, representing 2.5 mm of divergence under standard divergence velocities, and 7.5 mm of divergence under the high divergence velocity in the second phase of Model D. The CT data are subsequently visually analyzed in Horos (https://horosproject.org/), an open source DICOM viewer software. Finally, selected CT sections from orthogonal rifting Models A and C are used for 2D DIC analysis in DaVis, providing the first-ever quantified insights in deformation of analogue models of lithospheric-scale rifting.

3. Results

3.1. Orthogonal rifting Model A

The orthogonal rifting model A involves a simulated lithosphere with half the standard thickness and no seed in the upper mantle layer. Results of this model, which is stretched at a divergence velocity of 10 mm/h during 150 minutes, are presented in Fig. 3. Topography analysis (Fig. 3a, b) reveals the development of significant boundary effects in the shape of (half-)grabens along the longitudinal sidewalls, whereas no surface deformation is visible in the centre of the model. Furthermore, these boundary effects are strongest towards the mid-point of the longitudinal sides.

The same general pattern of deformation is shown by the results of the DIC analysis (Fig. 3c, d). The cumulative maximum normal strain data (Fig. 3c) highlights that normal faulting is most active along the sidewalls, as was horizontal displacement, as illustrated by the cumulative horizontal displacement data (Dy in Fig. 3d). These Dy data in Fig. 3d also reveal that the regions immediately adjacent to the short ends of the model, close to where the short overlapping sidewalls moved apart, undergo some displacement. A further indication of this differential displacement is provided by the slight warping of the surface grid, visible in the background of the DIC results (Fig. 3c, d).

CT-imagery provides additional insights into the internal development of Model A (Fig. 3e, f). The layering within the simulated lithosphere is not readily visible, but the transition between the model lithosphere and model asthenosphere is (Fig. 3e). The final CT-section of Model A reveals the boundary effects normal faulting along the longitudinal sidewalls within the model lithosphere, and the rising of the model asthenosphere (Fig. 3f).

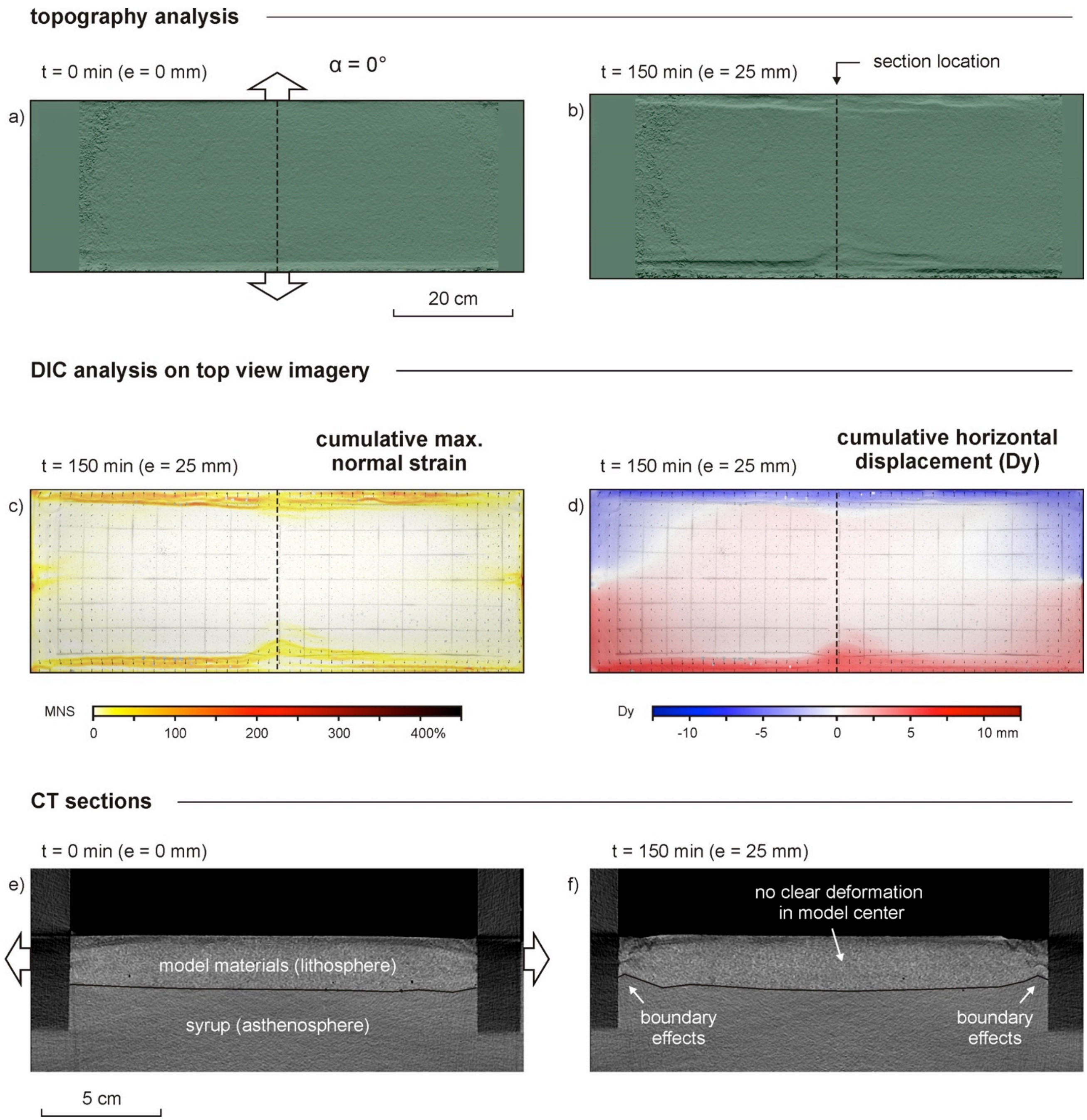

Fig. 3. Overview of results from Model A, with a modelled lithosphere of half the standard thickness and no seed, which underwent 10 mm/h orthogonal extension over a period of 150 min. (a-b) Topography analysis results, lighting from top. (c-d) DIC analysis. (c) Cumulative maximum normal strain (MNS) at the end of the model run, representing the length of the longest axis of the strain ellipse in the horizontal plane, which is taken as a proxy for normal fault development. (d) Cumulative horizontal displacement along the y-axis (parallel to the extension direction at the end of the model run. (e-f). CT-analysis on vertical sections (e) t = 0 min, and (f) t = 150 min. Section location is indicated in (a-d).

3.2. Orthogonal rifting Model B

Model B involves a standard lithosphere thickness and a seed in the upper lithospheric mantle, and is stretched at a rate of 10 mm/h over 4 hours (Fig. 4). We analyse the model topography and surface deformation only, since the model is not CT-scanned.

The results from the topography analysis show how the model, in stark contrast to Model A (which lacked a seed), starts developing a slight central depression at the surface at about 60 min of deformation (Fig. 4d). After 75 min of deformation, two graben structures start to appear at the long ends of the model (Fig. 4c). At this point in time, technical issues with the camera rig prevented the acquisition of time-lapse imagery for ca. 90 min, hence subsequent topography data are only available from t = 180 min on (Fig. 4d). These topography data show the presence of a double graben system, flanking a central depression, as well as some deformation (boundary effects) along the longitudinal sidewalls. Both grabens are well developed, and their combined surface expression is fairly symmetrical, and remains so until the end of the model run (Fig. 4e).

The incremental normal strain data obtained from DIC analysis, highlights normal faulting over the preceding 5 mm of extension and reveals that the double graben system seen in the topography analysis is in fact already established at t = 60 min, and is initially somewhat better developed near the short ends of the model (Fig. 4h). The vectors displaying horizontal displacement in the DIC maps show that the central depression between the double grabens remains in place during the model run, whereas the materials on both side of the double graben system move steadily outward (Fig. 4f-j).

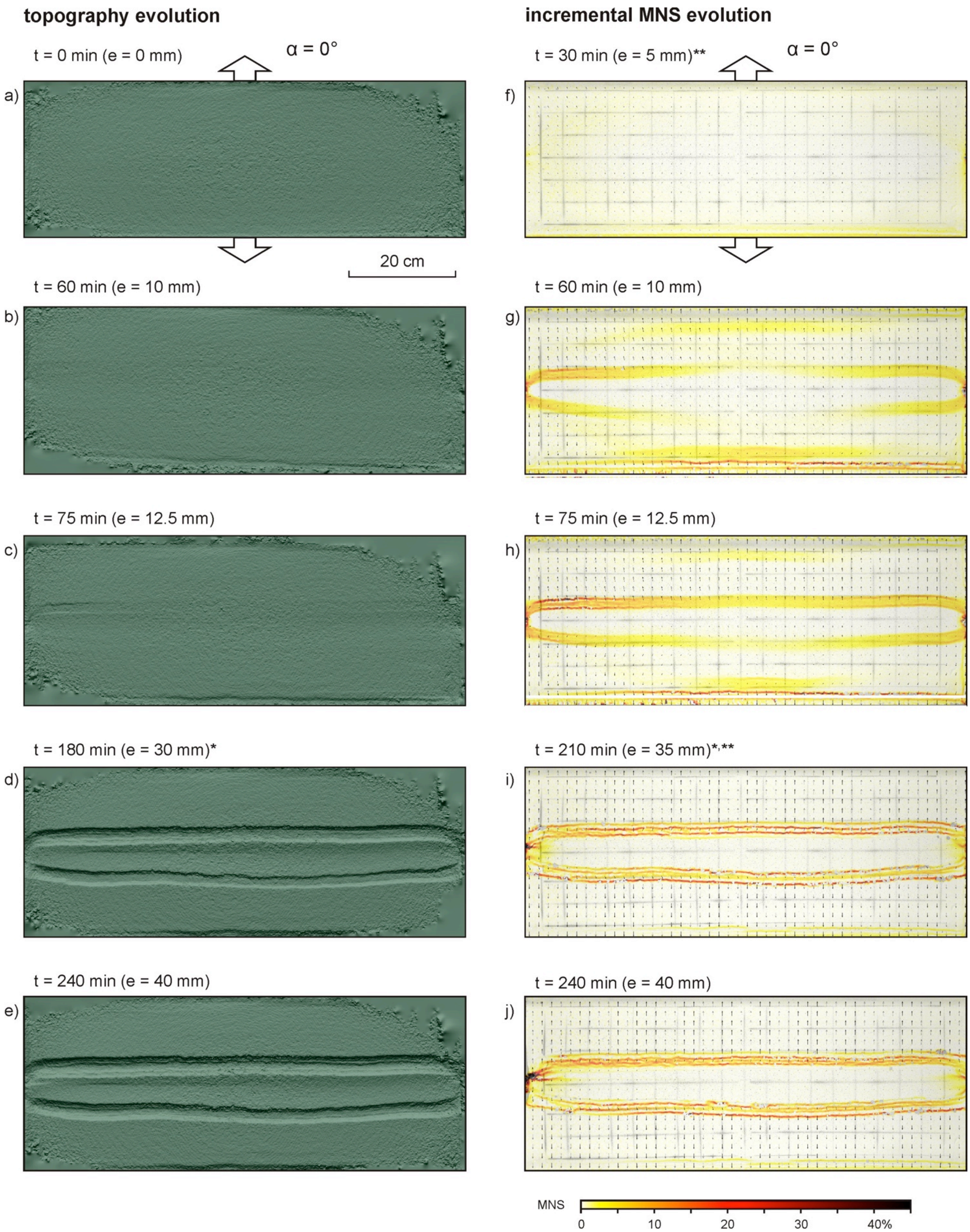

topography evolution
incremental MNS evolution
t = 0 min (e = 0 mm)
α = 0°
a)
20 cm
t = 60 min (e = 10 mm)
b)
t = 75 min (e = 12.5 mm)
c)
t = 180 min (e = 30 mm)*
d)
t = 240 min (e = 40 mm)
e)
t = 30 min (e = 5 mm)**
α = 0°
f)
t = 60 min (e = 10 mm)
g)
t = 75 min (e = 12.5 mm)
h)
t = 210 min (e = 35 mm)*,**
i)
t = 240 min (e = 40 mm)
j)
MNS
0
10
20
30
40%

Fig. 4. Topography and DIC analysis overview Model B (orthogonal rifting at a divergence velocity of 10 mm/h). (a-e) Topography analysis results, lighting from top. (f-j) DIC (incremental MNS [maximum normal strain]) analysis, representing the length of the longest axis of the strain ellipse in the horizontal plane, which is taken as a proxy for normal fault development. * Due to technical issues, no intermediate data were available between t = 75 min and t = 180 min. ** Due to DIC analysis requirements (an initial and deformed state is needed, and the analysis steps in this study are standardized to 5 mm of displacement), t = 30 min and t = 210 min are the first available data point at the start of the model, and after the data gap, respectively.

3.3. Orthogonal rifting Model C

3.3.1. Topography and model surface DIC analysis

The topography and DIC analysis results from Model C, which is a rerun of Model B monitored in the CT scanner, are presented in Fig. 5. Next to CT-scanning, we also perform the same topography and DIC analysis on Model C as done for Model B, allowing for a direct comparison between both models (Fig. 4). Furthermore, we use the CT-imagery for a qualitative assessment of model-internal deformation (Figs. 6, 7), as well as for a quantification of internal deformation through DIC analysis on CT sections (Fig. 8).

The topography analysis of Model C reveals a similar surface structure evolution as in Model B (Figs. 4a-e, 5a-e), with an initial central depression forming, followed by the development of grabens flanking this central depression. Like in Model B, the grabens are initially best developed towards the short ends of the model, before covering the whole length of the model (Fig. 5c-e). A major difference with Model B, however, is that the double graben arrangement in Model C is highly asymmetric to the short ends of the experiment (compare Figs. 4c-e and Figs. 5c-e). At the end of the model run both grabens in the central area of the model are about equally well developed with the upper graben accounting for the bulk of topography change towards the short ends of the model (Fig. 5e). Furthermore, some slight boundary effects are visible along the longitudinal sidewalls, as well as in the upper right corner of the model where some small additional grabens appear (Fig. 5e).

Similar to Model B, the DIC results of Model C shows how normal faulting starts localizing before structures are visible at the surface (at t = 60 min, Fig. 5b, g). The normal faulting initiates at the short ends of the model before growing towards the model centre, and is in fact rather symmetrical in the earlier stages of model evolution (Fig. 5g). Only later on, parts of the lower graben are abandoned so that the upper graben could become the dominant structure at the model surface (Fig. 5h-j). The DIC results highlight that the bulk of deformation is accounted for by the grabens in the model centre (Fig. 5f-j). The additional grabens in the upper right corner, as well as the boundary effects along the longitudinal sidewall, that are well visible on topography data (Fig. 5e), are shown to only localize minor amounts of normal faulting (Fig. 5f-j). An important detail is indicated by the displacement arrows: the central area between the double grabens is only (nearly) stationary (i.e. no vectors visible) where this area is flanked by two active grabens (Fig. 5f-j).

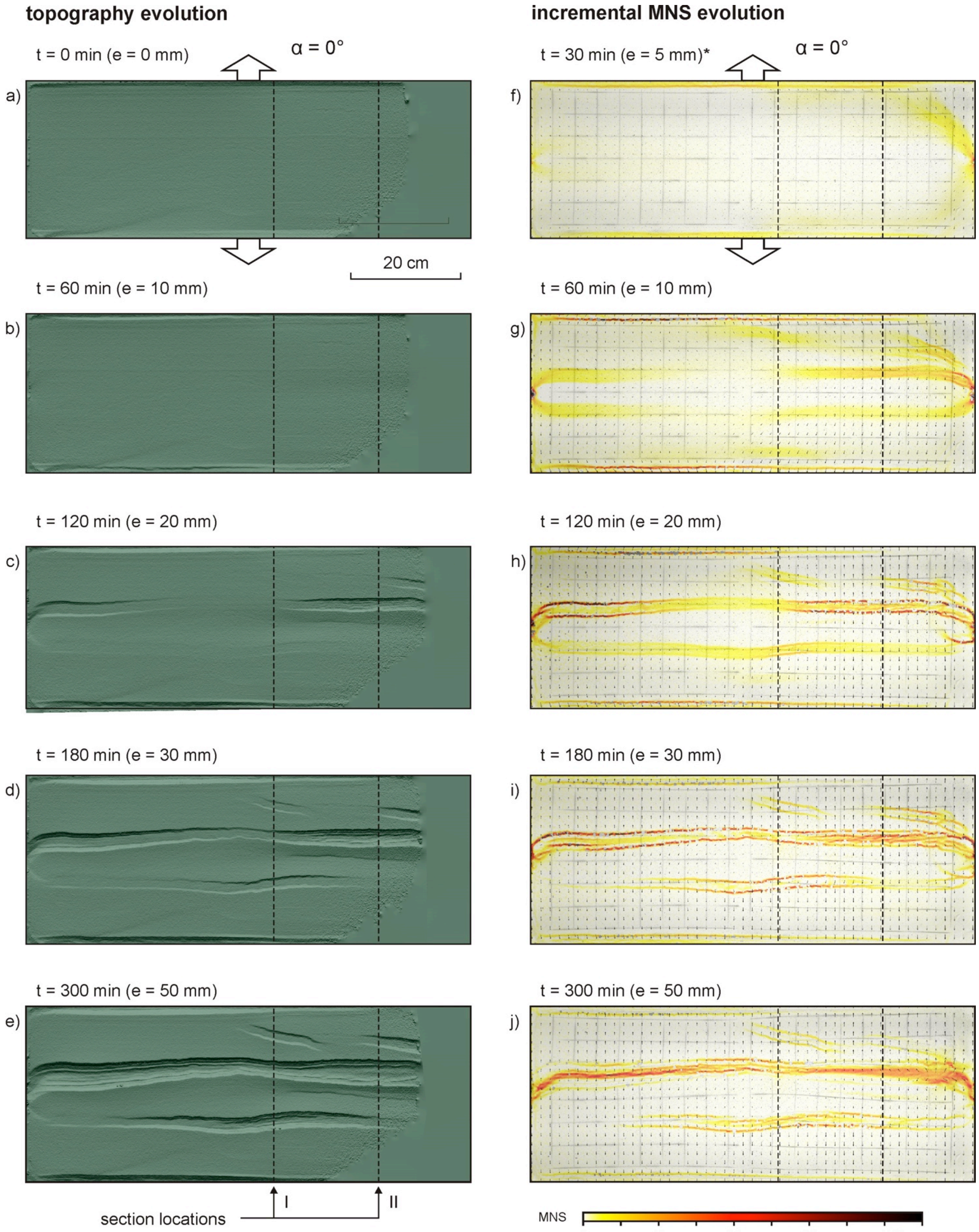

Fig. 5. Topography and DIC analysis overview Model C, which is a rerun of Model B (orthogonal rifting at a divergence velocity of 10 mm/h) completed in a CT scanner. (a-e) Topography analysis results, lighting from top. (f-j) DIC (incremental MNS [maximum normal strain]) analysis, representing the length of the longest axis of the strain ellipse in the horizontal plane, which is taken as a proxy for normal fault development. * Due to DIC analysis requirements (an initial and deformed state is needed, and the analysis steps in this study are standardized to 5 mm of displacement), t = 30 min is the first available data point after the start of the model run.

3.3.2. CT analysis

The acquisition of CT imagery and additional DIC analysis on CT-sections allows us to analyse the internal model evolution of Model C (Figs. 6, 7), with an emphasis on the differences between the symmetric and asymmetric rift structures previously identified by the topography and DIC analysis (Sections I and II, respectively, locations of which are shown in Fig. 5).

Section I, taken near the centre of Model C (Figs. 5a-e), shows the development a symmetric double rift structure (Figs. 6a-h, 7, a, c). In the earliest stages of rifting (t = 30 min, Fig. 6a), the seed in the simulated upper lithospheric mantle layer localizes deformation. As rifting progresses, this leads to the development of a graben structure in the upper lithospheric mantle with a central depression at the model surface (Figs. 6c, d, 7c). We subsequently observe the development of two upper crustal grabens flanking this central depression, which are linked to the graben in the upper lithospheric mantle by low angle shear zones (LASZs) in the simulated lower crust (Figs. 6e, 7c). At this point in time (t = 120 min), the upper lithospheric mantle layer is separated, and also a minor graben forms away from the central double graben structure (Fig. 6e). As rifting proceeds, this minor graben does not develop significantly, in contrast to the continuously developing double grabens (Figs. 6f-h, 7a, c). The rifting also leads to substantial thinning of the modelled lower crust (and of the model lithosphere in general), which is accommodated by the strong rise of the lower lithospheric mantle layer and the modelled asthenosphere, putting the lower lithospheric mantle and upper crust in near-direct contact (Figs. 6f-h, 7a).

Section II is taken ca. 20 cm away from Section I in Model C (Fig. 5a-e), and illustrates the development of an asymmetric double rift structure (Figs. 6i-p, 7b, d). Similar to Section I, initial deformation localizes in the upper lithospheric mantle layer (Fig. 6j). However, an early asymmetric transfer of deformation to the modelled upper crust causes the development of a graben on one side of the central model axis (Fig. 6k). As rifting continues and the upper lithospheric mantle becomes separated, this graben continues evolving (Figs. 6l, n, 7c, d). In the mean time, a smaller secondary graben appears on the other side of the central model axis, whereas a curved fault develops in the centre of the model (Fig. 6m, n). Another minor graben develops away from the central model axis as well (Fig. 6m, n). At this point in time (t = 120 min), the model asthenosphere and lower lithospheric mantle start to rise considerably, compensating the thinning lower mantle (and lithosphere in general) (Figs. 6n, 7b, d). As the model continues evolving, the initial graben remains dominant while the lithosphere continues thinning up to the point that the lower lithospheric mantle and upper crust are in contact (Fig. 6p, 7c, d). It is also worth noting how much the upper lithospheric mantle to the left in Section II is tilted upward when compared with the symmetric setting of Section I (Fig. 7c, d).

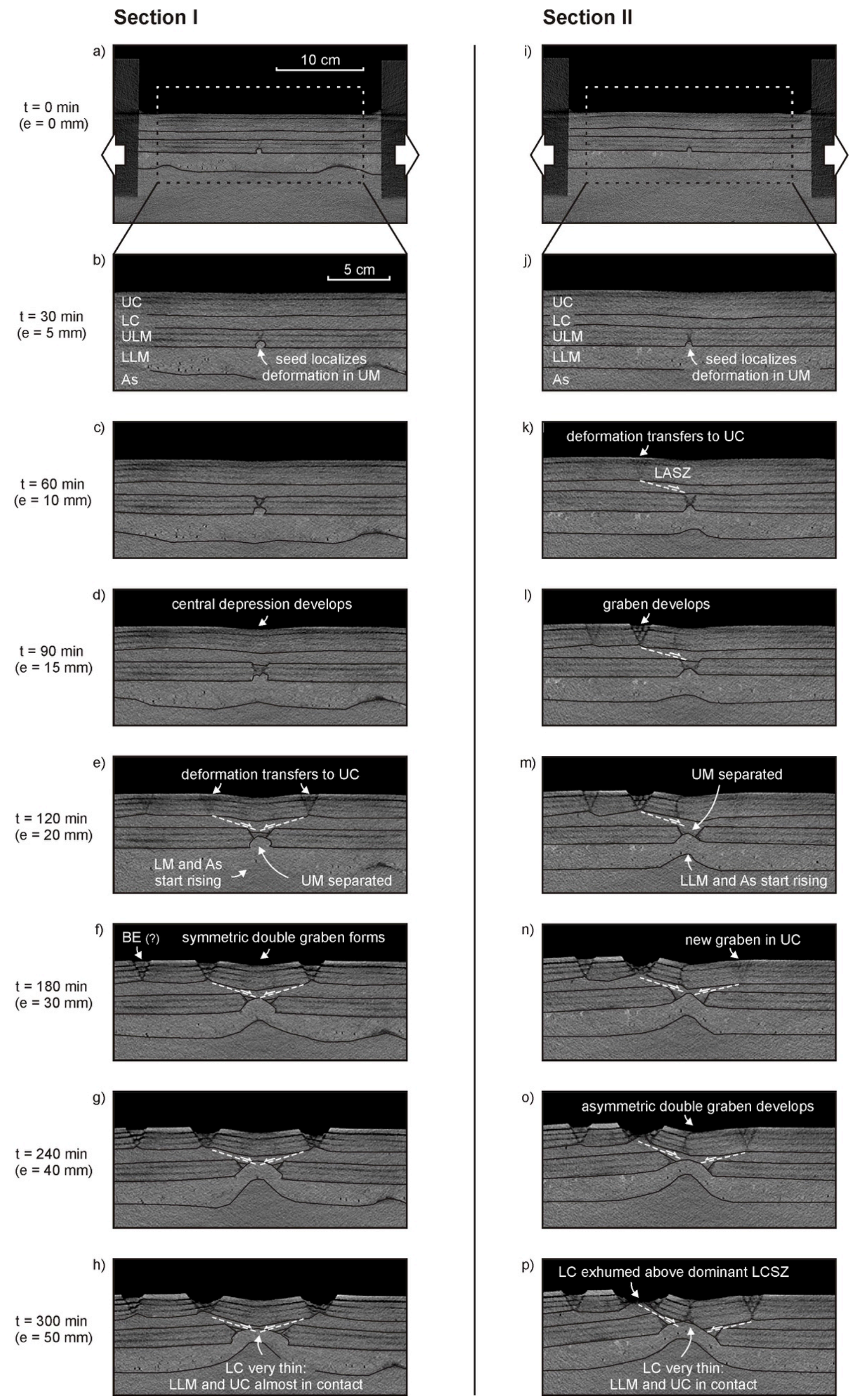

Fig. 6. CT sections I and II depicting the internal evolution of the symmetric and asymmetric double rift systems found in Model C. Dark lines are added to highlight layer contacts. LC: lower crust, LLC: lower lithospheric mantle. As: asthenosphere, LASZ: low-angle shear zone, LC: lower crust, LLM: lower lithospheric mantle, ULM: upper lithospheric mantle, UC: upper crust. CT section locations are indicated in Fig. 5.

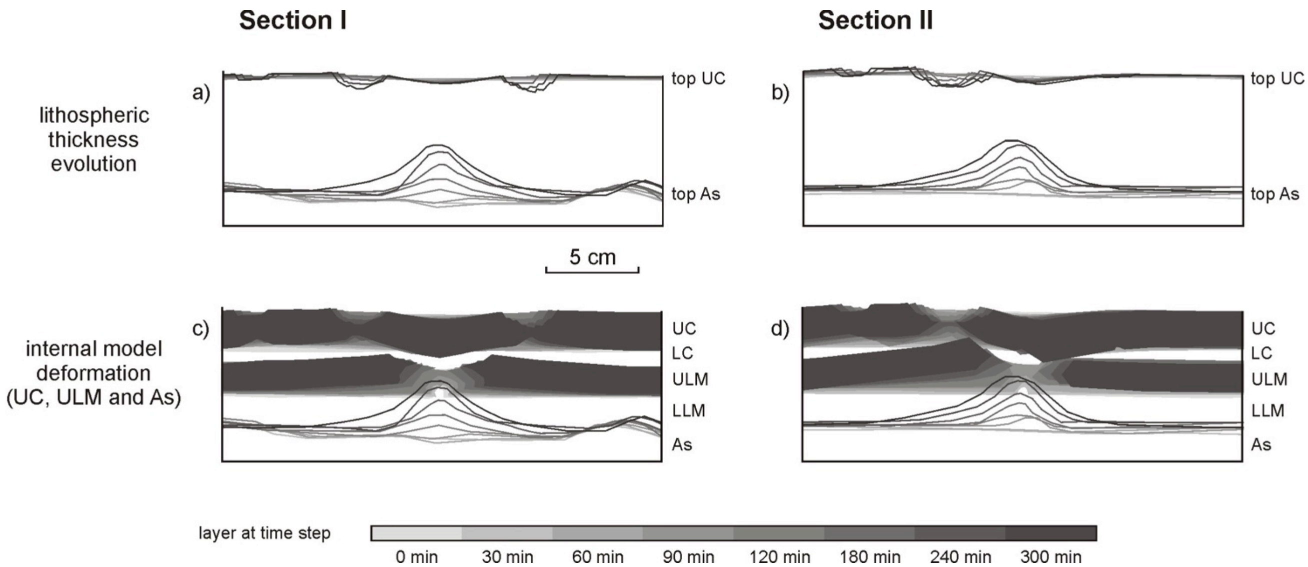

Fig. 7. Analysis of the internal evolution of symmetric and asymmetric rift structures seen on CT-sections I and II of Model C (Fig. 6), respectively. As: asthenosphere, LC: lower crust, LLM: lower lithospheric mantle, ULM: upper lithospheric mantle, UC: upper crust. (a-b) Horizon profiles charting the evolution of the model topography and the top of the asthenosphere layer. (c-d) Horizon profiles charting the evolution of the various layers in the lithosphere. Section locations are indicated in Fig. 5.

3.3.3. DIC analysis on 2D CT sections

In addition to visual inspection and interpretation of the CT imagery, we also apply DIC techniques to quantify model-internal deformation occurring in both Section I and II (Fig. 8). Firstly, cumulative horizontal displacement data (Dx) reveals the development of differences in Dx values over time in both Section I and II (Fig. 8a-d). The symmetric rift structure in Section I is characterized by a stationary upper crustal block between two lithospheric domains that are diverging (Fig. 8a, b). This arrangement is reminiscent of the stationary domain seen in DIC analysis of top view imagery in Models B and C (Figs. 4f-j, 5f-j). By contrast, the asymmetric rift structure in Section II lacks such a stationary domain, as the diverging domains are in direct contact (Fig. 8c, d). However, both sections have an additional low Dx domain in the lower part of the modelled lithosphere (Fig. 8a-d) Note that the boundaries between the different Dx domains in Sections I and II delineate the low-angle shear zones in the lower crust as identified on CT-imagery (Fig. 6h, p), as well as shear zones deeper in the lithosphere (Fig. 8a-d). In the case of the asymmetric rift structure in Section II, we observe a large-scale shear zone running through the whole lithosphere.

In addition to horizontal displacement values, we also present vertical displacement values (Dy) and cumulative vorticity obtained through DIC analysis (Fig. 8e-l). The Dy data reveal that the overall model lithosphere does not undergo significant vertical displacement (Fig. 8e-h), with the exception of the central rift zone, where the model surface is subsiding, and the asthenosphere is strongly rising (as also visible on the horizon profiles in Fig. 7). The cumulative vorticity data indicate changes in displacement patterns, highlighting shear zones in the model, as well as their sense of shear (Fig. 8i-l). Although they are not highly precise, the shear zones indicated by the cumulative vorticity results are in good agreement with those previously interpreted through the CT imagery and the Dx data (Figs. 6, 7, 8i-l).

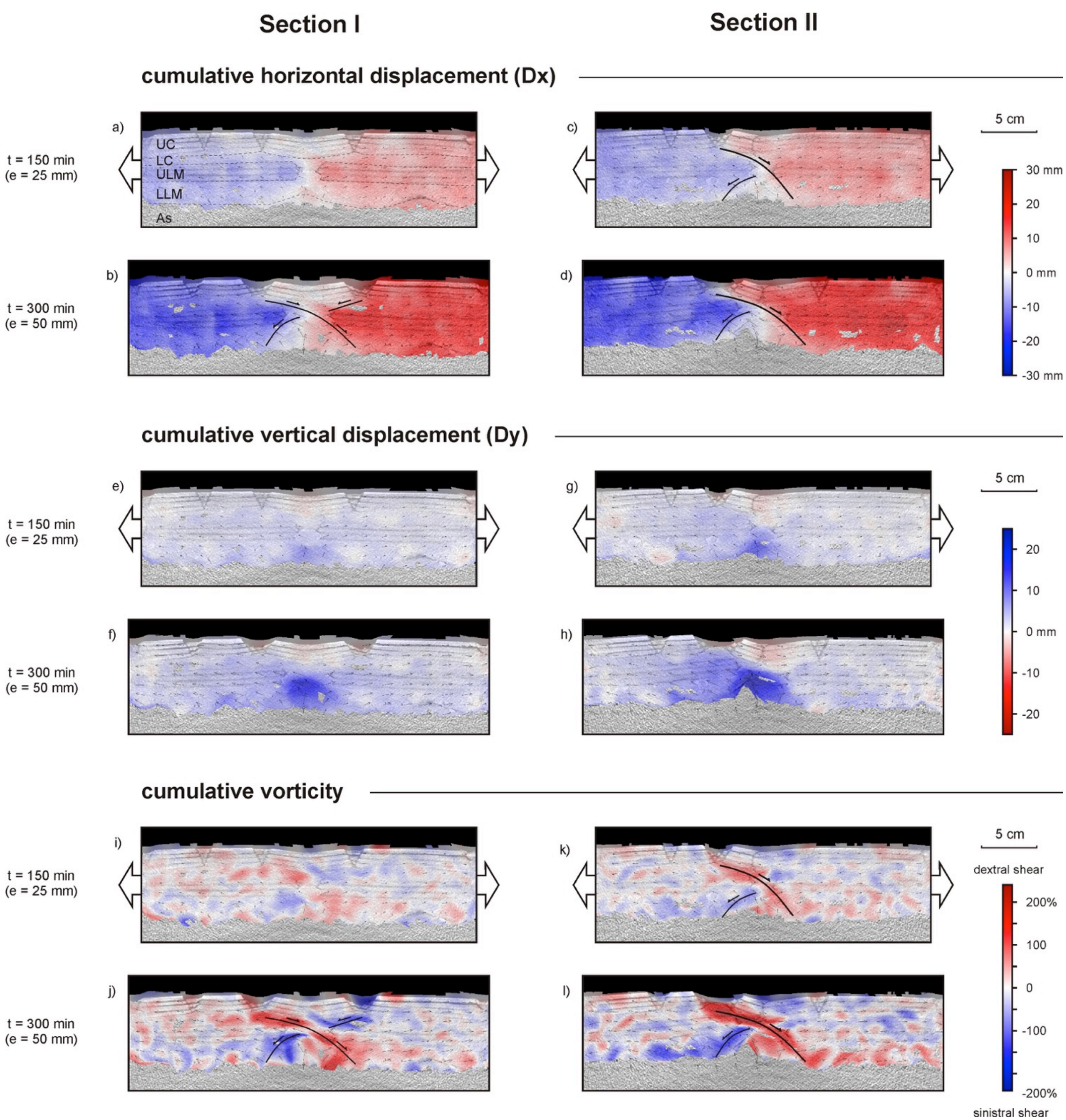

Fig. 8. Results of DIC analysis on CT sections I and II from Model C. (a-d) Cumulative horizontal displacement (Dx) (e-h) Cumulative vertical displacement (Dy). (k-l) Cumulative vorticity. Section locations are indicated in Fig. 5. As: asthenosphere, LC: lower crust, LLM: lower lithospheric mantle, ULM: upper lithospheric mantle, UC: upper crust.

3.4. Oblique rifting Model D

We present the topographic and surface DIC analysis of the 45° oblique rifting Model D in Fig. 9. During the first 195 min of deformation at the standard divergence rate of 10 mm/h, the model is being stretched and a depression formed along its central axis. At t = 180 min some faint deformation zones on both sides of this depression become visible on the DIC results (Fig. 9a-c, i-j). However, no clear faulting is observed, which is in clear contrast to the situation in orthogonal rifting Models B and C over the same period (Figs. 4a-d, f-i, 5a-d, f-i, 9a-c, i-j).

In order to force deformation in the model, we triple the divergence rate to 30 mm/h in the second phase of the model run, from t = 195 min on. As a result, faulting starts to localize along the deformation zones flanking the central depression (Fig. 9d-e, j-k). These faults are arranged in a left-stepping en echelon fashion, leading to the development of two zones of en echelon grabens along the central axis of the model, completed with a number of additional graben structures that are mostly located in the top-right corner (Fig. 9f). However, these additional grabens (as well as the boundary effects along the long ends of the model) only accommodate a minor part of the total deformation, as demonstrated by our DIC results (Fig. 9j-l)

CT imagery, presented in Fig. 10, provides insights into the internal deformation of Model D. The images show how during the first phase of the model run, deformation localizez along the seed, leading to the upper lithospheric mantle layer splitting apart (Fig. 10a-e). Yet, apart from some boundary effects along the long sidewalls, no clear faulting occurs in the upper crustal layer, as only the central depression seen on topography data develops (Figs. 9a-f, 10a-e). The situation totally changes during the second model phase as faster rifting led to the localization of faulting in the upper crustal layer, and the development of a symmetric double graben system (Fig. 10f-h). The en echelon nature of this double graben system, and its relation to the deformation deeper in the model lithosphere as well as the oblique divergence direction is revealed by 3D CT imagery (Fig. 10i).

Due to the lateral displacement component in Model D, the same 2D DIC analysis on CT sections as shown for orthogonal extension Model C was not performed. However, we may assume that the 2D cumulative displacement and deformation patterns in Model D are broadly similar to those obtained for Section I from Model C, given the similarity in CT section view (Figs. 6h, 10h).

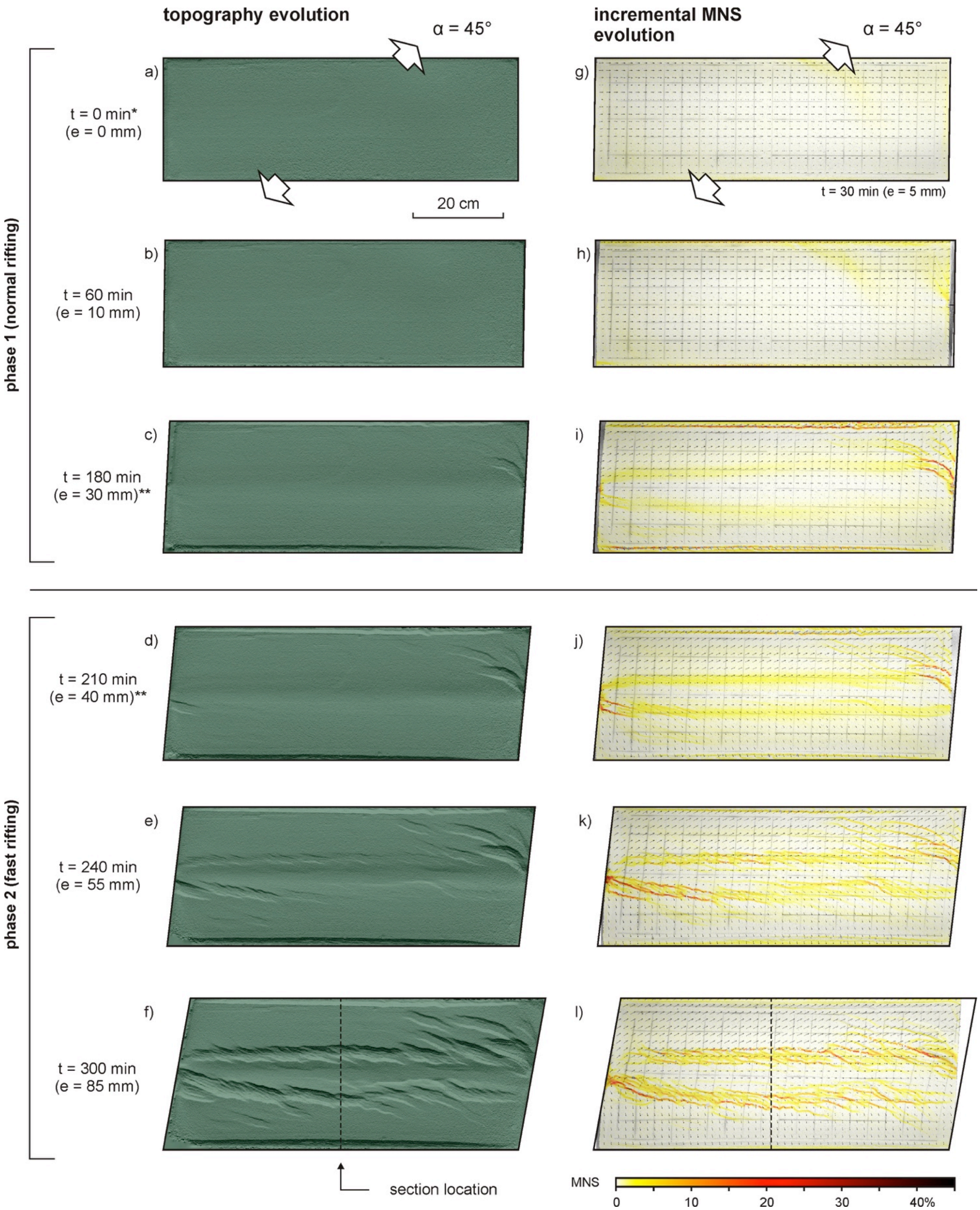

Fig. 9. Topography and DIC analysis overview of 45˚ oblique rifting Model D. (a-f) Topography analysis, lighting from top. (g-l) DIC (incremental maximum normal strain) analysis, representing the length of the longest axis of the strain ellipse in the horizontal plane, which is taken as a proxy for normal fault development.

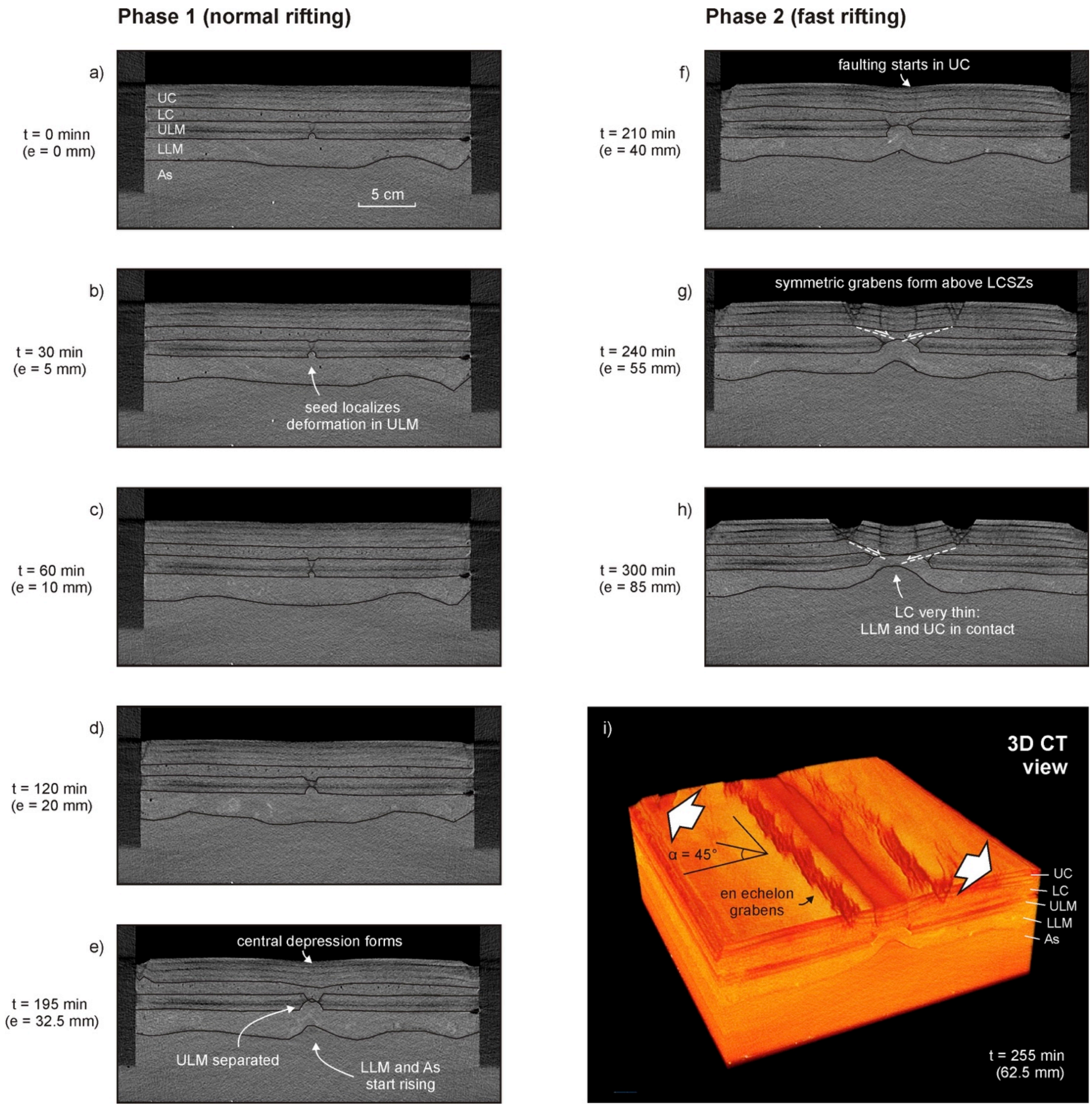

Fig. 10. CT analysis 45˚ oblique rifting Model D. (a-e). Model evolution in section view during phase 1 with the standard divergence velocity (10 mm/h). (f-h) Model evolution in section view during fast rifting phase 2 (30 mm/h). (i) 3D CT image at t = 255 min (62.5 mm of divergence). As: asthenosphere, LC: lower crust, LLM: lower lithospheric mantle, ULM: upper lithospheric mantle, UC: upper crust.

4. Discussion

Our model results obtained through a novel combination of external and internal monitoring and analysis techniques provide insights into three key topics: (1) the general localization of faulting, (2) symmetric and asymmetric rift systems, and (3) the development of rift systems in 3D through oblique extension. We summarize these results in text and figures (Figs. 11-13), and compare them with previous modelling results, before describing model limitations and potential implementations for our understanding of natural systems.

4.1. Localization of faulting: effects of seed and coupling

The first key observations concern the general localization of deformation in our models, as summarized in section view in Figure 11. The absence of deformation in the form of faulting in the upper crustal layer along the central axis of Model A without a seed, highlights that such a seed is required to localize a rift structure in this model set-up (compare Model A with Models B-C, Figs. 3-11a, c). The need for a seed or weakness to localize deformation in brittle-viscous set-ups has been shown by various previous analogue and numerical modellers (e.g. Zwaan et al. 2019; Oliveira et al. 2022), and is linked to the decoupling effect of the weak viscous layer representing the lower crust. This decoupling isolates the competent brittle layers in the model lithosphere, and deformation will simply focus along the sidewalls, which form the weakest part of the model, whereas the brittle layers simulating the upper crust and upper lithospheric mantle remain stationary and undeformed. However, in other analogue modelling studies of lithospheric-scale rifting, researchers induce deformation by using a narrower set-up with U-shaped sidewalls (e.g. Allemand & Brun 1991; Brun & Beslier 1996; Autin et al. 2010; Nestola et al. 2013, 2015). The edges of these U-shaped sidewalls act as velocity discontinuities (VDs), triggering deformation along the central model axis. But as pointed out by Zwaan et al. (2019), and even partiality visible at the short ends of our models as well (Fig. 5), faulting then tends to initiate at these VDs before growing towards the centre of the model.

Furthermore, our models show that divergence velocity affects the strength coupling between the competent (brittle) layers and plays an important role in the localization of faulting as well. Orthogonal rifting models B and C generates double graben structures due to a transfer of deformation from the seed in the upper lithospheric mantle through the lower crust into the upper crust (Figs. 6, 9). However, such transfer of deformation does not occur in (the initial phase of oblique rifting) Model D, where only a central depression forms, with some faulting along the sidewalls, whereas the upper lithospheric mantle layer split apart due to the presence of the seed (Figs. 10, 11b). This difference is likely (partially) caused by the orthogonal divergence velocity component (Y1+Y2, which determines the amount of new area created in the system) during the first phase of Model D being smaller than in Models B and C (Table 3). As a result of this lower divergence velocity in Model D, the strength of the lower crustal layer, which has a strain-rate dependent rheology, is reduced. Therefore, the upper lithospheric mantle and upper crustal layers are more decoupled and localized deformation cannot be transferred between both these competent layers (e.g. Brun 1999, 2002; Zwaan et al. 2019). Vice versa, faster rifting, as in phase 2 of Model D, increases coupling, leading to the initiation of faulting in the upper crustal layer due to transfer of localized deformation from the seed upward, whereas faulting along the sidewalls is reduced (Fig. 10, 11c). These findings are in accordance with previous modelling work showing that faster divergence allows (localized) deformation in the mantle to have more influence on upper crustal faulting, or to even overprint and suppress deformation otherwise occurring along weaknesses in the upper crust, leading to complex interactions and rift structures (Zwaan et al. 2021a, 2021b).

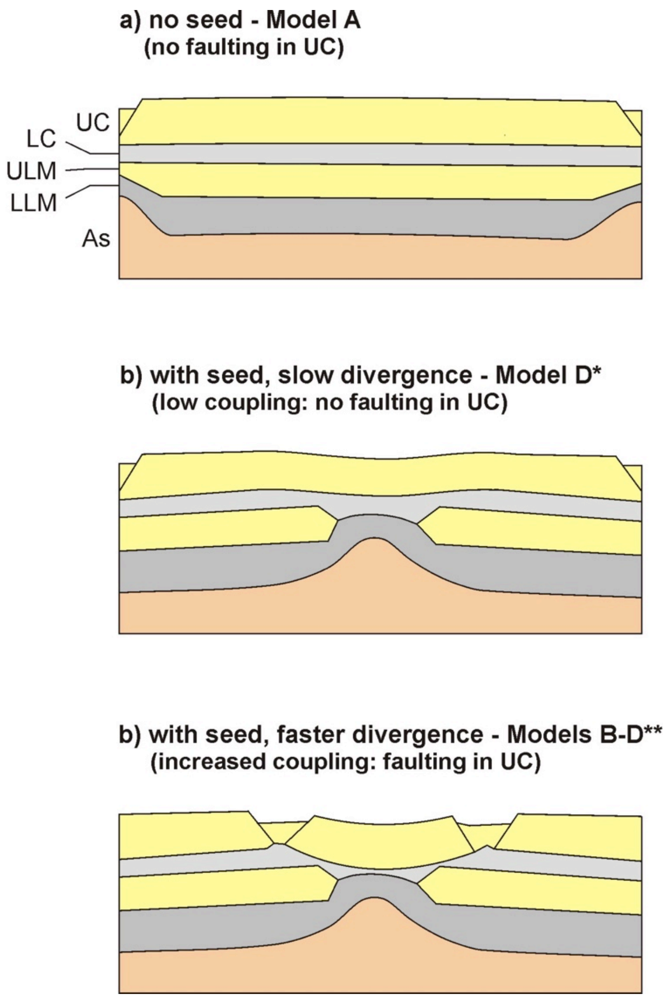

Fig. 11. Schematic 2D overview of how seeds and the degree of coupling between the competent upper crust and upper lithospheric mantle (as a function of divergence velocity that affects the strength of the lower crustal layer) influences model development. As: asthenosphere, LC: lower crust, LLM: lower lithospheric mantle, ULM: upper lithospheric mantle, UC: upper crust. (a) Situation in Model A, without seed and moderate divergence velocity, leading to the development of boundary effects only. (b) Situation during the first phase of Model D, with a seed but relatively slow divergence and a weaker lower crust, leading to low coupling so that the deformation in the upper lithospheric mantle does not induce faulting in the upper crustal layer. Instead, upper crustal faulting occurs in the shape of boundary effects along the longitudinal sides of the model. (c) Situation in Model B and C (with a seed and moderate divergence velocities) or in the second phase of Model D (with a seed and a high divergence velocity), leading to a stronger lower crust and sufficient coupling to transfer deformation from the upper lithospheric mantle into the upper crustal layer and to induce faulting there.

4.2. Symmetric vs. asymmetric rift development

The orthogonal rifting Models B and C, both with seeds, provide important insights in the development of symmetric and asymmetric rift structures, as summarized in section view in Fig. 12.

Both Models B and C show the development of symmetric rift structures as a result of symmetric transfer of deformation from the seed in the competent lithospheric mantle into the upper crustal layer (Figs. 4, 5, Section I in Figs. 6-8, 12). As described in the preceding paragraph, a degree of coupling related to a moderate divergence rate is needed for this deformation transfer, which occurs along two shear zones in the lower crustal layer. The development of such double shear zones has been observed in both lithospheric-scale analogue models (e.g. Brun & Beslier 1996; Michon & Merle 2000; 2003, Nestola et al. 2014), as well as in crustal-scale brittle-viscous models, where instead of a seed the edge of a base plate (VD) represents a fault in the upper lithospheric mantle (e.g. Allemand et al. 1989; Zwaan et al. 2019; 2021a, 2021b). Moreover, they are also observed in numerical modelling studies (Dyksterhuis et al. 2007; Chenin et al. 2018; 2020, Oliveira et al. 2022). In the case of a symmetric rift structure, two of these shear zones form simultaneously on both sides of the seed, causing the development of two equally sized grabens in the upper crustal layer, with a relatively undeformed “H-block” (i.e. “hanging wall block”, Lavier & Manatschal 2006; Péron-Pinvidic & Manatschal 2010) in between (Fig. 12b, c).

By contrast, in some parts of Model C, the rift structure develops in an asymmetric fashion (Fig. 5, Section II in Figs, 6-8, 12). In this asymmetric system we find the early development of a single shear zone in the lower crust, inducing a single graben in the upper crust early on (Fig. 12e). In later stages, a second shear zone may develop, but the initial shear zone stays dominant and evolves into a large shear zone crossing the whole lithosphere, whereas the lower crust is exhumed at the bottom of the dominant graben (Fig. 12f). It is not clear why this asymmetry occurs in (parts of) Model C, especially since the structures in Model B are fully symmetrical (Fig. 4). The analogue models by Allemand et al. (1989) provide a possible explanation, suggesting that the basal boundary condition (symmetric or asymmetric deformation by means of a brittle-viscous base plate setup, and the plate edge [VD] simulating deformation in the upper lithospheric mantle) may cause such differences in rift style. A problem with this explanation is that our basal boundary condition is in principle symmetric, and brittle-viscous models with a VD, and asymmetric deformation do not always develop asymmetric rifts (Zwaan et al. 2021a, 2021b). Also Brun & Beslier (1996) showed the development of an asymmetric rift structure in their asymmetric setup, with the difference that their reported model evolution involves an initial symmetric rift style, followed by a shift to an asymmetric rift style. However, since their cross-sections are taken from different models with different amounts of extension, it may be possible that their rift evolution scenario mixes observations from both symmetric and asymmetric rift systems. We therefore speculate that the set-up we applied in our models is close to a tipping point, so that small differences in model preparation, which are known to affect analogue modelling results (e.g. Schreurs et al. 2006, 2016), may locally shift the system from a symmetrical to an asymmetrical style, and vice versa. Indeed, numerical modelling studies show that a variety of factors can affect the symmetry of a rift system (e.g. Huismans & Beaumont 2002, 2003; Nagel & Buck 2004; Huismans et al. 2005; Brune et al. 2014), but a detailed comparison of our analogue models with these numerical results is beyond the scope of this paper.

However, even though we cannot pinpoint with surety what causes this shift in rift style in this study, our new models allow us to examine and compare both symmetric and asymmetric rifting situations. In both cases we find a sharp rise of the asthenosphere, isostatically compensating the strong thinning of the lithosphere, which in the centre chiefly consists of upper crustal and lower lithospheric mantle material as both the lower crust and upper lithospheric mantle are practically split in two (Figs. 6h, p, 7, 12c, d). This rise of the asthenosphere is a universal observation in other lithospheric-scale analogue and numerical models undergoing strongly localized thinning (e.g. Allemand et al. 1989; Brun & Beslier 1996, Nestola et al. 2013, 2015; Brune et al. 2014; Chenin et al. 2018, 2020), and prevents the local "collapse" of the modelled lithosphere that may occur in advanced stages of rifting if no such istostatic compensation is included. Furthermore, there is no unrealistic regional subsidence of undeformed parts of the lithosphere due to stretching of the model and viscous thinning of lower crustal layer, previously observed in two-layer brittle-viscous models (e.g. Zwaan et al. 2020; Schmid et al. 2022a).

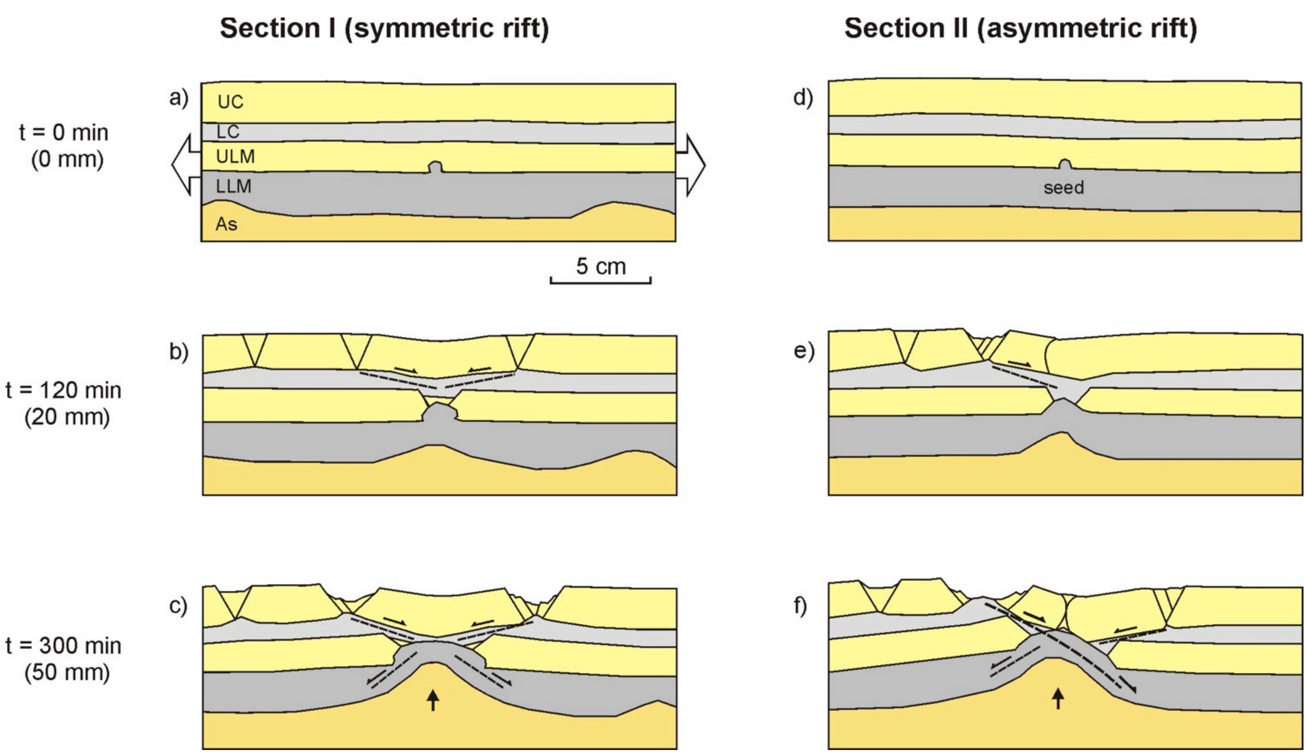

Fig. 12. Schematic evolution of (a-c) symmetric vs. (d-f) asymmetric rift systems (right), based on CT imagery from Model C (Fig. 6). As: asthenosphere, LC: lower crust, LLM: lower lithospheric mantle, ULM: upper lithospheric mantle, UC: upper crust.

4.3. Oblique extension and 3D rifting structures

Apart from purely 2D considerations detailed in the previous sections, our orthogonal and oblique rifting models also provide insights in 3D deformation (summarized in Fig. 13). Our orthogonal extension Models B and C generate symmetric and asymmetric rift systems with through-going faults parallel to the model axis of the models (Figs. 4, 5, 13a, b). By contrast, our oblique extension Model D, after developing only limited faulting in the upper crust during the initial phase, forms two series of obliquely oriented basins during the second, faster extension phase (Figs. 9, 10i, 13c).

These series of left-stepping en echelon basins follow in fact the trace of the double grabens in the orthogonal extension situation (Fig. 13a). This indicates that, after increasing the divergence velocity in the second phase of Model D, the lower crust is sufficiently strong to allow for the development of shear zones in the lower crust that transfer deformation (coupling) from the seed in the upper lithospheric mantle into the upper crustal layer (Fig. 13a).

Within this framework, the en echelon faults themselves are typical of oblique extension systems, as normal faults form perpendicular to the (local) extension direction (which itself may deviate from the plate divergence direction in oblique divergence settings, Withjack & Jamison 1986). Examples of en echelon faulting in oblique divergence settings are found in lithospheric-scale analogue and numerical models (e.g. Autin et al. 2010, 2013; Agostini et al. 2009; Brune 2014; Duclaux et al. 2020), as well as in crustal scale experiments (e.g. Tron & Brun 1991; McClay & White 1995; Zwaan et al. 2021a, 2021b). Zwaan et al. (2021a, 2021b), applying a brittle-viscous base plate set-up also reproduce the double graben style with en echelon faulting, indicating that some aspects of lithospheric-scale models (i.e. deformation in the crustal parts) can be well-represented by simpler models

Finally, even though not observed in our study, there is a good possibility that, similar to their orthogonal extension counterparts, oblique divergence models could develop asymmetric rift systems with a single zone of en echelon faulting (Fig. 13d). As in the case of the orthogonal divergence models, an asymmetric rift under oblique divergence conditions would lead to earlier exhumation of the lower crust than in the symmetric equivalent. However, this exhumation would itself be delayed compared to the lower crustal exhumation in the orthogonal extension models, due to the smaller orthogonal divergence component (Y1+Y2) in our models (Table 3, Fig. 13). This is somewhat in contradiction to the numerical models by Brune et al. (2012), who suggested that oblique extension promotes continental break-up.

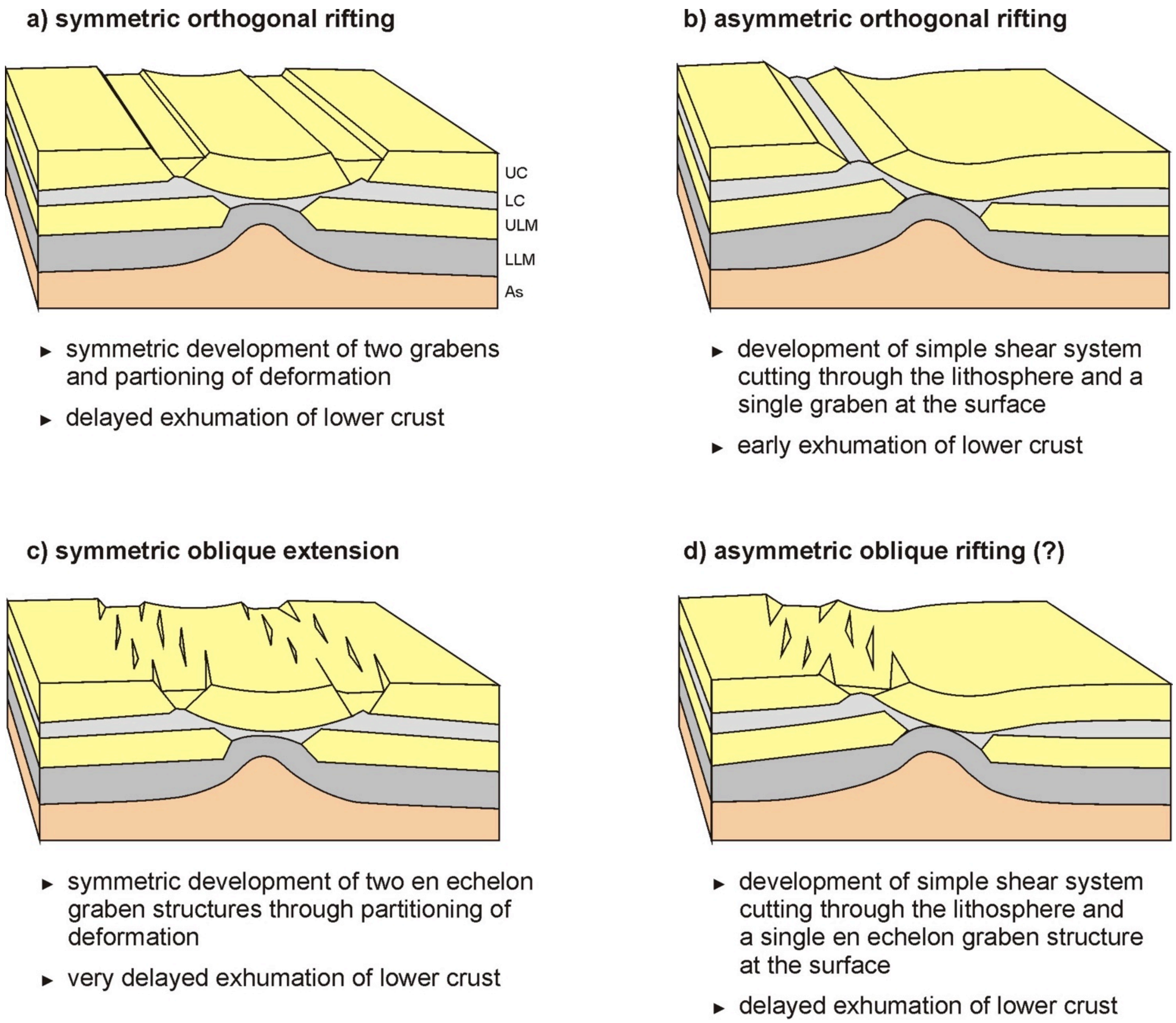

Fig. 13. 3D sketches of final model results, depicting the difference between rift structures developing in (a) a symmetric orthogonal extension system (Models B, C), (b) an asymmetric orthogonal extension system (parts of Model C), (c) (fast) symmetric oblique rifting (Model D), and (d) the expected result of a model with (fast) symmetric oblique rifting. As: asthenosphere, LC: lower crust, LLM: lower lithospheric mantle, ULM: upper lithospheric mantle, UC: upper crust.

4.3. Model limitations, and opportunities for improvement and new studies

Our novel application of CT-scanning as well as subsequent DIC analysis on CT-imagery is a significant step forward in the field of analogue modelling. Firstly, it provides us with unprecedented insights into the internal deformation evolution of lithospheric-scale rifting models (Figs. 6, 7, 10). Especially the quantification of deformation over time in these models allows for direct comparisons with numerical modelling studies. However, the CT-scanning resolution (512 x 512 Px) forms a limitation. The imagery allows for excellent visual inspection and interpretation, but the resolution is relatively low for detailed DIC analysis. This limitation could however be mitigated to a degree by applying (industrial) CT-scanners with higher resolution, by selecting a smaller scan window, or by applying thicker model layering. As a matter of fact, the 8 cm thick lithosphere we apply is already much thicker than in most other analogue modelling studies, and has been intentionally increased to improve the resolution of our results. We estimate that a further doubling of this lithospheric thickness would be feasible.

The new set-up and general modelling approach itself has also proven itself to be successful. However, the procedure is somewhat challenging due to the limitation imposed by the requirements for CT-scanning: the materials need to be X-ray transparent, and the whole set-up needs to fit into a CT-scanner. As a result, the syrup basin is relatively small, so that adding the relatively thick lithosphere risks causing large displacement of syrup, in contrast to other modelling set-ups that either have much larger basins or much thinner lithospheres. Our solution to freeze the syrup for stability during model preparation means that completing a single model takes a week, limiting the modelling output (Zwaan & Schreurs 2022b). This lower output is however more than offset by the CT-scanning results, and it will be possible to prepare multiple models in parallel to double or triple the modelling output. Furthermore, this new set-up allows for easy simulation of different degrees of oblique divergence, and as such the study of 3D tectonic processes in rift systems.

A further consideration is the lithospheric layering and model materials. Various authors have applied different lithospheric layering (e.g. Allemand et al. 1989), and we have only explored a very small part of the potential parameter space. Rerunning models with these different types of lithospheric layering would allow for new insights. A limitation in most analogue models of lithospheric-scale rifting has always been that most materials generally do not undergo thermal effects. This may not be much of an issue in models such as those presented in this paper, which mainly aim at the earlier stages of rifting when thermal effects are considered of minor importance (Zwaan et al. 2021a, 2021b). However, as the lithosphere starts necking, and the hot asthenosphere starts rising to the surface (Figs. 6, 7, 9, 12), we should expect phase changes and variations in rheology to kick in. Therefore, the inclusion of model materials, of which the rheology is affected by temperature changes (e.g. Chemenda et al. 2002; Boutelier & Oncken 2011; Boutelier et al. 2012), in CT-scanned models of lithospheric-scale rifting would be a promising avenue for future studies. This could be combined with parallel numerical modelling efforts, which will allow for both benchmarking and verification of both modelling methods (e.g. Panien et al. 2006; Zwaan et al. 2016; Brune et al. 2017), and for the addition of other parameters that are challenging to include in lithospheric-scale analogue models (e.g. surface processes). In this context, it is also important to stress that the current method is only suitable for the modelling of magma-poor continental break-up, since magmatism can strongly affect rift evolution (e.g. Buck 2004; 2006).

Finally, we see great opportunities beyond the field of rifting, as our new method could also be applied for the simulation of (oblique) collisional tectonics (e.g. Willingshofer & Sokoutis 2009; Luth et al. 2010; Sokoutis & Willingshofer 2011; Willingshofer et al. 2013; Calignano et al. 2015; 2017) and lithospheric-scale basin inversion (Cerca et al. 2005; Gartrell et al. 2005).

4.4. Application of model results to interpret natural rift systems

Even though our analogue modelling efforts are not directly designed to represent a specific natural case, they provide some insights into the evolution of (magma-poor) rifts in nature. Firstly, our models show the importance of coupling in rift systems, where high coupling between the competent mantle and crustal layers via a relatively strong lower crust allows deformation in the mantle to strongly affect deformation in the (upper) crust (Fig. 11). The effects of such coupling between the competent layers in extensional systems is well known from nature, where low coupling due to a weak and thick post-collisional lower crustal layer can lead to core complex formation, as for instance observed in the Basin and Range province (e.g. Brun et al. 2017). By contrast, high coupling can lead to narrow rifting if deformation is strongly localized in the mantle, such as is the case for the Rhine Graben and Baikal Rift (e.g. Allemand & Brun 1991), whereas distributed deformation in the mantle in combination with high coupling causes a wide rifting style in the crust (Brun 1999, 2002, Zwaan et al. 2021b). The models in this paper involve moderate coupling with localized deformation in the mantle leading to double rift systems, and a natural example of such systems could be the Eastern and Western Troughs of the North Sea Central Graben (e.g. Hodgson et al. 1992; Erratt 1999).

Secondly, our models provide insights into the development of (magma-poor) symmetric and asymmetric rift systems and importantly, how an asymmetric rift system may develop from the earliest phases on (Fig. 12). This seems somewhat in contrast with the scenario proposed by e.g. Lavier & Manatschal (2006) for magma-poor rifts, in which continental rifting initiates with a symmetric phase (pure shear rifting, McKenzie 1978), before lithospheric-scale asymmetric break-up takes over (simple shear rifting, Wernicke 1985). Our modelling results (as well as the numerical work by Brune et al. 2014) suggest that such a shift may not be required to initiate asymmetric rifting, but does not deny the possibility of such shifts. If we furthermore project the evolution of symmetric and asymmetric rift systems, we predict that the former case would lead to delayed mantle exhumation, due to the localization of uplift below two grabens in the upper crust (Fig. 14c). In the latter case however, deformation is focussed in one graben, allowing for early exhumation of the lower crust, and we can subsequently expect early mantle exhumation as well (Fig. 14d). Moreover, direct exhumation of the mantle at the original necking site is likely prevented by the presence of relatively undeformed crustal materials there (i.e. the H-block). Instead, mantle exhumation should be expected to occur away from the original necking location (Fig. 14b, d), which is in fact observed in nature (e.g. Unternehr et al. 2010; Péron-Pinvidic & Manatschal 2010).

Finally, we can apply our oblique extension model results for a comparison with natural examples. The en echelon structures in our Model D may be similar to those in the aforementioned North Sea Central graben, which exhibits various en echelon graben arrangements that are indicative of oblique extension (e.g. Erratt et al. 1999; 2010). As the system contains both double grabens and single grabens along its axis, there may also be shifts between symmetric and asymmetric oblique divergence (Fig. 13c, d). The evolution of the North Sea rift system is indeed a contested issue, and analogue models can help shed light on this topic (e.g. Zwaan et al. 2021a, 2021b).

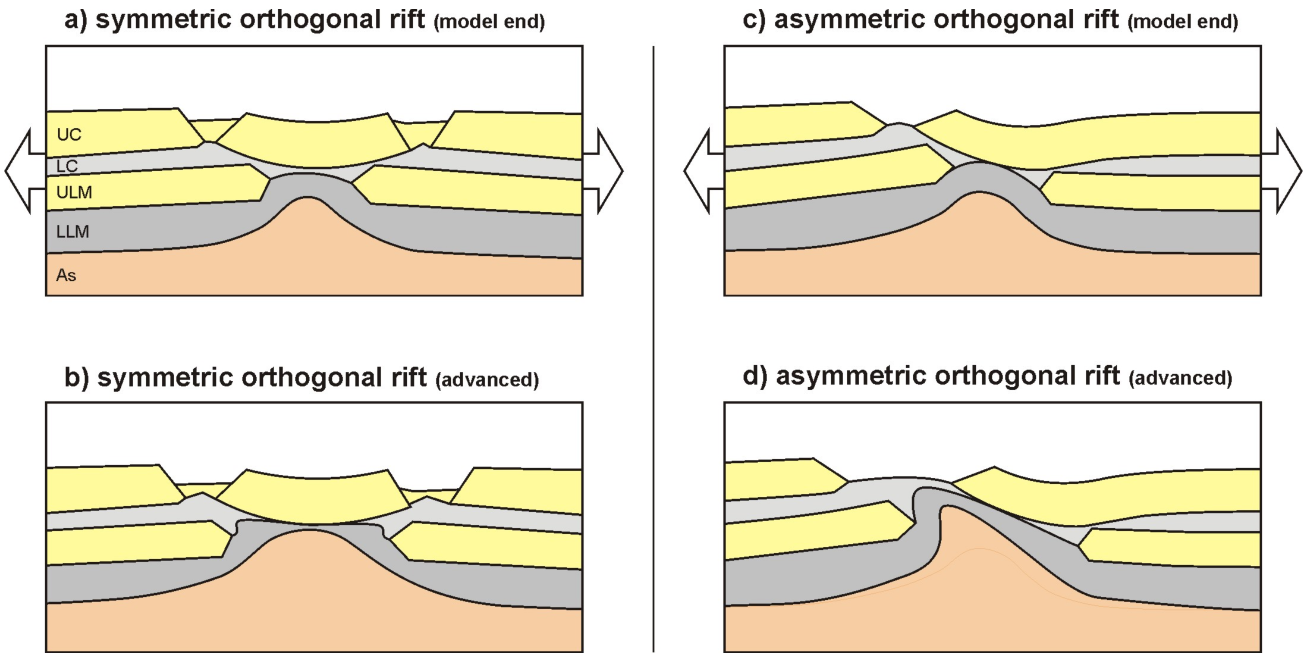

Fig. 14. Prediction of the advanced evolution of symmetric and asymmetric rift systems, based on the final state of Model C (see also Fig. 12). As: asthenosphere, LC: lower crust, LLM: lower lithospheric mantle, ULM: upper lithospheric mantle, UC: upper crust.

5. Conclusion and future outlook

In this paper we present a novel method for the modelling of (magma-poor) lithospheric-scale rifting processes, which can be uniquely monitored in a CT-scanner. We show how the application of CT-scanning and DIC analysis on CT imagery provides unparalleled insights into the development of rift systems. Our models provide also the following insights into the development of rift systems:

- The degree of coupling between the competent layers in the lithosphere in the presence of a weak lower crust has an important influence on the development of rift systems. Low coupling due to slow rifting isolates the upper crust from the upper lithospheric mantle layer below, preventing an efficient transfer of deformation between both layers. By contract, fast rifting increases coupling and allows deformation in the mantle to efficiently induce deformation in the upper crust.

- When sufficient coupling occurs and deformation is transferred from the mantle into the upper crust, we observe either the development of a symmetric or asymmetric (double) rift system. The reason why the system may develop one or the other style is not fully clear, however our models show that asymmetric deformation may initiate during the earliest phases of continental break-up. This is in contrast to the two-phase scenario involving initial symmetric deformation (pure shear), followed by asymmetric deformation (simple shear) during break-up.

- Oblique divergence leads to en echelon graben arrangements, and a delayed exhumation of lower crustal and, eventually, mantle material. This is somewhat in contradiction to the concept of oblique divergence promoting break-up.

These insights provide an incentive to further simulate rifting processes on lithospheric scales, and to apply advanced techniques to extract as much information as possible out of these. There is indeed a broad range of opportunities for improvements to our new modelling method, e.g. involving the testing of different lithospheric layering and the inclusion of new materials with temperature-sensitive rheology, for new studies within and beyond the field of rift tectonics.

Acknowledgements

We would like to thank the engineers from IPEK Rapperswil (Dario Niggli, Peter Eichenberger, Theodor Wüst) for working out our initial design and for constructing the components for the new model set-up. We are grateful to Nicole Schwendener from the Institute of Forensic Medicine in Bern for helping us scan our models. Thanks also to Timothy Schmid from our Tectonic Modelling group for helping with the DIC analysis, and to Kirsten Elger from GFZ Potsdam for helping us prepare the GFZ data publications containing the supplementary data of this paper (Schmid et al. 2022; Zwaan & Schreurs 2022a, b, and Zwaan et al. 2022). This project was funded by the Swiss National Science Foundation, grant 200021-178731 "4D Analogue modelling of oblique rifts and obliquely rifted margins"(http://p3.snf.ch/Project-178731), and the University of Bern covered the Open Access publication costs.

Data availability statement

Supplementary material is available in the form of publicly accessible data publications, stored at the servers of GFZ Data Services. New details on the material properties of the glucose syrup and feldspar sand used in these models can be found in Schmid et al. 2022b (LINK*), and Zwaan et al. 2022 (LINK*). Videos depicting the evolution of the model results and analyses (both in surface view and in [CT] section view) are provided in Zwaan & Schreurs 2022a (LINK*). Detailed background on the modelling method itself can be found in Zwaan & Schreurs 2022b (LINK*).

(*) as soon as the manuscript will be accepted for publication, the data publications will be finalized and published on the GFZ Dataservices website (Incl. DOI link). Example of GFZ data publication: https://doi.org/10.5880/fidgeo.2018.072. The data in the data publications is already available via the DropBox links added to the 4 citations in the reference list.

Appendix A1. Model Scaling

Applying analogue modeling scaling laws (e.g. Hubbert 1937; Ramberg 1981; Weijermars & Schmeling 1986) demonstrates the suitability of our models for simulating continental rifting processes. The parameters for our scaling calculations are provided in Table A1.

The standard length scaling ratio (h*) in our models was $6.7 \cdot 10^{-7}$ (ratio convention: model/nature), so that 1 cm correspond to 15 km in nature, and the whole 6.5 cm thick model layering represents a ca. 100 km thick lithosphere. The density ratio (ρ*) and gravity ratio (g*) were ca. 0.45, and 1 in our models, respectively. Using these data we obtained the stress ratio (σ*) via the following equation (Hubbert 1937; Ramberg 1981): $\sigma^* = \rho^* \cdot h^* \cdot g^*$. Here ρ*, h* and g* represent the density, length and gravity ratios respectively, and the equation yields a σ* of ca. $3 \cdot 10^{-7}$.

For brittle materials, scaling is relatively straightforward due to their strain-rate independent rheology. Most important is the internal friction angle of the feldspar sand we used, which is very similar that of upper crustal rocks (e.g. Byerlee, 1978, Table A1). The dynamic similarity in the brittle layers can be validated by calculating the Rs ratio (Ramberg 1981; Mulugeta 1988; Bonini et al., 2001): Rs = gravitational stress/cohesive strength = $(\rho \cdot g \cdot h) / C$. Here ρ is the density, g the gravitational acceleration, h the height and C cohesion of the brittle materials. Our calculations yield Rs values for the upper crust and upper lithospheric mantle that very similar between model and nature (Table A1), confirming the adequate dynamic scaling of the brittle behavior of the materials in our models.

Scaling of viscous materials is more complex due to their strain-rate dependent rheology. In the case of viscous materials, the stress ratio (σ*) and viscosity ratio (η*) produce the strain rate ratio (ε*) according to the ensuing formula: $\dot{\varepsilon}^* = \sigma^* / \eta^*$ (Weijermars & Schmeling 1986), which is in the order of $1 \cdot 10^{10}$. Subsequently, we can obtain the velocity ratio v* and time ratios t* through the following equations: $\dot{\varepsilon}^* = v^*/h^* = 1/t^*$. As a result, our standard divergence velocity of 10 mm/h translates to ca. 3.2 mm/yr in nature, which is similar to divergence rates observed in nature (e.g. Saria et al. 2014).

To test dynamic similarity of the viscous layers, we apply the Ramberg number Rm (Weijermars & Schmeling 1986): $Rm = (\rho \cdot g \cdot h^2) / (\eta \cdot v)$. The Rm values obtained for the different viscous layers in our models are very similar to the Rm values for their natural counterparts (Table A1). Together with the Rs values the Ramberg numbers indicate that scaling requirements are reasonably fulfilled for our standard model runs.

In the case of Model A, with half the layer thickness, the scaling is still adequate, but the divergence rate of 10 mm/h, translates to 11 mm/yr. In the case of the enhanced divergence velocity in Model D, scaling remains according to the standard model parameters in Table A1, except that the 30 mm/h divergence velocity during the second model phase translates to 9.6 mm/yr. These divergence velocities of 11 and 9.6 mm/yr are somewhat at the high end in nature. However, in the case of Model A did not significantly affect model evolution due to the decoupling between the model layers and the lack of a seed, whereas the increased coupling was needed in Model D to force localization. In the case of Model D, a slower divergence (e.g. 15

mm/h, translating to 4.8 mm/yr) could also have sufficed, but we chose to somewhat force the system in order to obtain a result.

Table A1: Scaling details (for standard model parameters)

		Model	**Nature**
General parameters	Gravitational acceleration (g)	9.81 m/s^2	9.81 m/s^2
	Divergence velocity (v)*	$2.7 \cdot 10^{-6}$ m/s	$2.5 \cdot 10^{-9}$ m/s
Upper crust (UC)	Material	Feldspar sand	Upper crustal rocks
	Peak internal friction angle (φ)	35°	30-38°
	Thickness (h)	$2 \cdot 10^{-2}$ m	$3 \cdot 10^{4}$ m
	Density (ρ)	1300 kg/m^3	2800 kg/m^3
	Cohesion (C)	51 Pa	$1.6 \cdot 10^{8}$ Pa
Lower crust (LC)	Material	Viscous mixture 1	Lower crustal rocks
	Thickness (h)	$1 \cdot 10^{-2}$ m	$1.5 \cdot 10^{4}$ m
	Density (ρ)	1300 kg/m^3	2900 kg/m^3
	Viscosity (η)	$6 \cdot 10^{4}$ Pa·s	$1 \cdot 10^{22}$ Pa·s
Upper Lithospheric mantle (ULM)	Material	Feldspar sand	Peridotite
	Peak internal friction angle (φ)	35°	30-38°
	Thickness (h)	$1.5 \cdot 10^{-2}$ m	$2.25 \cdot 10^{4}$ m
	Density (ρ)	1300 kg/m^3	3300 kg/m^3
	Cohesion (C)	51 Pa	$2 \cdot 10^{8}$ Pa
Lower Lithospheric mantle (LLM)	Material	Viscous mixture 2	Peridotite
	Thickness (h)	$2 \cdot 10^{-2}$ m	$3 \cdot 10^{4}$ m
	Density (ρ)	1400 kg/m^3	3400 kg/m^3
	Viscosity (η)	$8 \cdot 10^{4}$ Pa·s	$1.2 \cdot 10^{22}$ Pa·s
Asthenosphere	Material	Glucose syrup	Peridotite
	Thickness (h)	-	-
	Density (ρ)	1450 kg/m^3	3300 kg/m^3
	Viscosity (η)	65 Pa·s	$9 \cdot 10^{18}$ Pa·s
Dynamic scaling values	Brittle stress ratio (R_s)		
	UC	5.2	5.2
	ULM	3.75	3.5
	Ramberg number (R_m)		
	LC	7.2	7.1
	LLM	6.2	6.1
	As	$7.9 \cdot 10^{3}$	$7.9 \cdot 10^{3}$

* Model B with standard extension rate of 10 mm/h, translating to 3.2 mm/yr in nature for the scaling values presented in this table.

References

Allemand, P., & Brun, J. -P. (1991). Width of continental rifts and rheological layering of the lithosphere. Tectonophysics, 188, 63-69. https://doi.org/10.1016/0040-1951(91)90314-I

Allemand, P., Brun, J. -P., Davy, P., & Van den Driessche, J. (1989). Symétrie et asymétrie des rifts et mécanismes d'amincissement de la lithosphere. Bulletin de la Société Géologique de France, V(3), 423-436. https://doi.org/10.2113/gssgfbull.V.3.423

Alonso-Henar, J., Schreurs, G., Martinez-Díaz, J. J., Álvarez-Gómez, J. A., & Villamor, P. (2015). Neotectonic development of the El Salvador Fault Zone and implications for deformation in the Central America Volcanic Arc: Insights from 4-D analog modeling experiments. Tectonics, 34, 133–151. https://doi.org/10.1002/2014TC003723

Agostini, A., Corti, G., Zeoli, A., & Mulugeta, G. (2009). Evolution, pattern, and partitioning of deformation during oblique continental rifting: Inferences from lithospheric-scale centrifuge models. Geochemistry, Geophysics, Geosystems, 10, Q11015. https://doi.org/10.1029/2009GC002676

Autin, J., Bellahsen, N., Husson, L, Beslier, M.-O., Leroy, S., & d'Acremont, E. (2010). Analog models of oblique rifting in a cold lithosphere, Tectonics, 29, TC6016. https://doi.org/10.1029/2010TC002671

Autin, J., Bellahsen, N., Leroy, S., Husson, L., Beslier, M.-O.-M., & d'Acremong, E., (2013). The role of structural inheritance in oblique rifting: Insights from analogue models and application to the Gulf of Aden. Tectonophysics, 607, 51-64. https://doi.org/10.1016/j.tecto.2013.05.041

Bahroudi, A., Koyi, H. A., & Talbot, C.J. (2003). Effect of ductile and frictional de´collements on style of extension. Journal of Structural Geology, 25, 1401-1423. https://doi.org/10.1016/S0191-8141(02)00201-8

Beniest, A., Willingshofer, E., Sokoutis, D., & Sassi, W. (2018). Extending continental lithosphere with lateral strength variations: effects on deformation localization and margin geometries. Frontiers in Earth Science, 6, 148. https://doi.org/10.3389/feart.2018.00148

Beslier, M. -O. (1991). Formation des marges passives et remontée du manteau : Modélisation expérimentale et exemple de la marge de la Galice. Memoires et documents du Centre Armoricain d'etude structurale des socle, (Doctoral Dissertation). Retrieved from HAL (https://tel.archives-ouvertes.fr/tel-00594598). University Rennes 1, France.

Benes, V., & Davy, P. (1996). Modes of continental lithospheric extension: experimental verification of strain localization processes. Tectonophysics, 254, 69-87. https://doi.org/10.1016/0040-1951(95)00076-3

Benes, V., & Scott, S.D. (1996). Oblique rifting in the Havre Trough and its propagation into the continental margin of New Zealand: comparison with analogue experiments. Marine Geophysical Researches, 18, 189-201.

https://doi.org/10.1007/BF00286077

Biggs, J., Ayele, A., Fischer, T. P., Fontijn, K., Hutchison, W., Kazimoto, E., Whaler, K., & Wright, T. J. (2021). Volcanic activity and hazard in the East African Rift Zone. Nature Communications, 12, 6881. https://doi.org/10.1038/s41467-021-27166-y

Bonechi, N., Fiaschi, D., Manfrida, L., Talluri, L., & Zuffi, C. (2021). Exploitation assessment of geothermal energy from African Great Rift Valley. E3S Web of Conferences, 312, 08008. https://doi.org/10.1051/e3sconf/202131208008

Bonini, M., Sokoutis, D., Mulugeta, G., Boccaletti, M., Corti, G., Innocenti, F., Manetti, P., & Mazzarini, F. (2001). Dynamics of magma emplacement in centrifuge models of continental extension with implications for flank volcanism. Teconics, 20(6), 1053-1065. https://doi.org/10.1029/2001TC900017

Boutelier, D., & Oncken, O. (2011). 3-D thermo-mechanical laboratory modeling of plate-tectonics: modeling scheme, technique and first experiments. Solid Earth, 2, 35-51. https://doi.org/10.5194/se-2-35-2011

Brun, J. -P. (1999). Narrow rifts versus wide rifts: inferences for the mechanics of rifting from laboratory experiments. Philosophical Transactions of the Royal Society, London, A, 357, 695-712. https://doi.org/10.1098/rsta.1999.0349

Brun, J. -P. (2002). Deformation of the continental lithosphere: Insights from brittle-ductile models. Geological Society, London, Special Publications, 200, 355-370. https://doi.org/10.1144/GSL.SP.2001.200.01.20

Brun, J. -P., & Beslier, M.-O. (1996). Mantle exhumation at passive margins. Earth and Planetary Science Letters 142, 161-173. https://doi.org/10.1016/0012-821X(96)00080-5

Brun, J. P., Sokoutis, D., Tirel, C., Gueydan, F., Van Den Driessche, J., & Beslier, M.-O. (2018). Crustal versus mantle core complexes. Tectonophysics, 746, 22-45. https://doi.org/10.1016/j.tecto.2017.09.017

Brune, S. (2014). Evolution of stress and fault patterns in oblique rift systems: 3-D numerical lithospheric-scale experiments from rift to breakup. Geochemistry, Geophysics, Geosystems, 15, 392-3415. https://doi.org/10.1002/2014GC005446

Brune, S. (2016). Rifts and rifted margins: a review of geodynamic processes and natural hazards. In J. C. Duarte, & W. P. Schellart (Eds.), Plate Boundaries and Natural Hazards, 13-37. https://doi.org/10.1002/9781119054146.ch2

Brune, S., Popov, A. A., & Sobolev, S. V., (2012). Modeling suggests that oblique extension facilitates rifting and continental break-up, Journal of Geophysical Research, 117, B08402. https://doi.org/10.1029/2011JB008860

Brune, S., Heine, C., Pérez-Gussinyé, M., & Sobolev, S. V. (2014). Rift migration explains continental margin asymmetry and crustal hyper-extension. Nature Communications, 5, 4014. https://doi.org/10.1038/ncomms5014

Brune, S., Corti, G., & Ranalli, G. (2017). Controls of inherited lithospheric het- erogeneity on rift linkage: Numerical and analog models of interaction between the Kenyan and Ethiopian rifts across the Turkana depression, Tectonics, 36, 1767–1786 https://doi.org/10.1002/2017TC004739

Buck, R. W. (2004). Consequences of asthenospheric variability on continental rifting. In G. Karner, B. Taylor, N. Driscoll, & D. Kohlstedt (Eds.), *Rheology and Deformation of the Lithosphere at Continental Margins*, 1-29. https://doi.org/10.7312/karn12738-002

Buck, R. W. (2006). The role of magma in the development of the Afro-Arabian Rift System. Geological Society, London, Special Publications, 259, 43-54. https://doi.org/10.1144/GSL.SP.2006.259.01.05

Burnside, N., Montcoudiol, N., Becker, K., & Lewi, E. (2020). Geothermal energy resources in Ethiopia: Status review and insights from hydrochemistry of surface and groundwaters. *Wiley Interdisciplinary Reviews: Water*, 8(6), e1554. https://doi.org/10.1002/wat2.1554

Byerlee, J. (1978). Friction of Rocks. Pure and Applied Geosphysics, 116(4-5), 615-626. https://doi.org/10.1007/BF00876528

Calignano, E., Sokoutis, D., Willingshofer, E., Gueydan, F., & Cloetingh, S. (2015). Asymmetric vs. symmetric deep lithospheric architecture of intra-plate continental orogens. Earth and Planetary Science Letters, 424, 38-50. https://doi.org/10.1016/j.epsl.2015.05.022

Calignano, E., Sokoutis, Willingshofer, E., Brun, J.-P., Gueydan, F., & Cloetingh, S. (2017). Oblique contractional reactivation of inherited heterogeneities: Cause for arcuate orogens. Tectonics, 36, 542-558. https://doi.org/10.1002/2016TC004424

Capelletti, A., Tsikalas, F., Nestola, Y., Cavozzi, C., Argnani, A., Meda, M., & Salvi, F. (2013). Impact of lithospheric heterogeneities on continental rifting evolution: Constraints from analogue modelling on South Atlantic margins. Tectonophysics, 608, 30-50. https://doi.org/10.1016/j.tecto.2013.09.026

Catuneanu, O., Abreu, V., Bhattacharya, J. P., Blum, M.D., Dalrymple, R.W., Eriksson, P.G., et al. (2009). Towards the standardization of sequence stratigraphy. Earth-Science Reviews, 92, 1-33. https://doi.org/10.1016/j.earscirev.2008.10.003

Catuneanu, O., & Zecchin, M. (2013). High-resolution sequence stratigraphy of clastic shelves II: Controls on sequence development. Marine & Petroleum Geology 39, 26-38. https://doi.org/10.1016/j.marpetgeo.2012.08.010

Chemenda, A., Déverchère, J., & Calais, E. (2002). Three-dimensional laboratory modelling of rifting: application to the Baikal Rift, Russia. Tectonophysics 356, 253-273. https://doi.org/10.1016/S0040-1951(02)00389-X

Chenin, P., Schmalholz, S. M., Manatschal, G., & Karner, G. D. (2018). Necking of the lithosphere: A reappraisal of basic concepts with thermo-mechanical numerical modeling. *Journal of Geophysical Research: Solid Earth*, *123*. https://doi.org/10.1029/2017JB014155

Chenin, P., Schmalholz, S. M., Manatschal, G., & Duretz, T. (2020). Impact of crust–mantle mechanical coupling on the topographic and thermal evolutions during the necking phase of 'magma-poor' and 'sediment-starved' rift systems: A numerical modeling study. Tectonophysiscs, 786, 228472. https://doi.org/10.1016/j.tecto.2020.228472

Cerca, M., Ferrari, L., Corti. G., Bonini, M., & Manetti, P. (2005). Analogue model of inversion tectonics explaining the structural diversity of Late Cretaceous shortening in southwestern Mexico. Lithosphere, 2, 172-187.
https://doi.org/10.1130/L48.1

Colletta, B., Letouzey, J., Pinedo, R., Ballard, J. F., & Balé, P. (1991). Computerized X-ray tomography analysis of sandbox models: Examples of thin-skinned thrust systems. Geology, 19(11), 1063-1067. https://doi.org/10.1130/0091-7613(1991)019<1063:CXRTAO>2.3.CO;2

Corti, G. (2008). Control of rift obliquity on the evolution and segmentation of the main Ethiopian rift. Nature Geoscience, 1, 258-262.
https://doi.org/10.1038/ngeo160

Corti, G. (2012). Evolution and characteristics of continental rifting: Analog modeling-inspired view and comparison with examples from the East African Rift System. Tectonophysics, 522-523, 1-33. https://doi.org/10.1016/j.tecto.2011.06.010

Corti, G., Bonini, M., Conticelli, S., Innocenti, F., Manetti, P., & Sokoutis, D. (2003). Analogue modelling of continental extension: a review focused on the relations between the patterns of deformation and the presence of magma. Earth-Science Reviews, 63, 169-247.
https://doi.org/10.1016/S0012-8252(03)00035-7

Corti, G., Ranalli, G., Agostini, A., & Sokoutis, D. (2013). Inward migration of faulting during continental rifting: Effects of pre-existing lithospheric structure and extension rate. Tectonophysics, 594, 137-148.
http://dx.doi.org/10.1016/j.tecto.2013.03.028

Duclaux, G., Huismans, R. S., & May, D. A. (2020). Rotation, narrowing, and preferential reactivation of brittle structures during oblique rifting. Earth and Planetary Science Letters, 531, 115952. https://doi.org/10.1016/j.epsl.2019.115952

Dyksterhuis, S., Rey, P., Müller, R.D., & Moresi, L. (2007). Effects of initial weakness on rift architecture. Geological Society, London, Special Publication, 282, 443–455.
https://doi.org/10.1144/SP282.18

Erratt, D., Thomas, G. M., & Wall, G. R. T. (1999). The evolution of the Central North Sea Rift. Geological Society, London, Petroleum Geology Conference series, 5, 63-82.
https://doi.org/10.1144/0050063

Erratt, D., Thomas, G. M., Hartley, N.R., Musum, R., Nicholson, P.H., & Spisto, Y. (2010). North Sea hydrocarbon systems: some aspects of our evolving insights into a classic hydrocarbon province. Geological Society, London, Petroleum Geology Conference series, 7, 37-56.
https://doi.org/10.1144/0070037

Fedorik, J., Zwaan, F., Schreurs, G., Toscani, G., & Bonini, L. (2019). The interaction between strike-slip dominated fault zones and thrust belt structures: Insights from 4D analogue models. Journal of Structural Geology, 122, 89-105. https://doi.org/10.1016/j.jsg.2019.02.010

Freymark, J., Sippel, J., Scheck-Wenderoth, M., Bär, K., Stiller, M., Fritsche, J. -H., & Kracht, M. (2017). The deep thermal field of the Upper Rhine Graben. Tectonophysics, 694, 114-129. https://doi.org/10.1016/j.tecto.2016.11.013

Gartrell, A., Hudson, C., & Evans, B. (2005). The influence of basement faults during extension and oblique inversion of the Makassar Straits rift system: Insights from analog models. American Association of Petroleum Geologists Bulletin, 89(4), 495-506. https://doi.org/10.1306/12010404018

Gouin, P. (1979). Earthquake history of Ethiopia and the Horn of Africa. International Development Research Centre, Ottawa, Canada.
Haq, B. U., Hardenbol, J., & Vail, P. R. (1987). Chronology of Fluctuating Sea Levels since the Triassic. *Science*, *235*(4793), 1156–1167. http://www.jstor.org/stable/1698241

Hodgson, N.A., Farnsworth, J., & Fraser, A.J. (1992). Salt-related tectonics, sedimentation and hydrocarbon plays in the Central Graben, North Sea, UKCS. Geological Society, London, Special Publications, 67, 31-63. https://doi.org/10.1144/GSL.SP.1992.067.01.03

Holland, M., van Gent, H., Balzalgette, L., Yassir, N., Hoogerduijn Strating, E. H., Urai, J. L. (2011). Evolution of dilatant fracture networks in a normal fault — Evidence from 4D model experiments. Earth and Planetary Science Letters, 304, 399–406. https://doi.org/10.1016/j.epsl.2011.02.017

Hubbert, M.K. (1937). Theory of scale models as applied to the study of geologic structures. Geological Society of America Bulletin, 48(10), 1459-1520. https://doi.org/10.1130/GSAB-48-1459

Huismans, R. S., & Beaumont, C. (2002). Asymmetric lithospheric extension: The role of frictional plastic strain softening inferred from numerical experiments. Geology, 30(3), 211-214. https://doi.org/10.1130/0091-7613(2002)030<0211:ALETRO>2.0.CO;2

Huismans, R. S., Buiter, S. J. H., & Beaumont, C. (2005). Effect of plastic-viscous layering and strain softening on mode selection during lithospheric extension. Journal of Geophysical Research, 110, B02406. https://doi.org/10.1029/2004JB003114

Kirschner, J. P., Kominz, M. A., & Mwakanyamale, K. E. (2010). Quantifying extension of passive margins: Implications for sea level change. Tectonics, 29, TC4006. https://doi.org/10.1029/2009TC002557

Klinkmüller, M. (2011). Properties of analogue materials, experimental reproducibility and 2D/3D deformation quantification techniques in analogue modeling of crustal-scale processes, (Doctoral dissertation). Location: University of Bern, Switzerland.

Koyi, H. (1997). Analogue modelling: from a qualitative to a quantitative technique – a historical outline. Journal of Petroleum Geology, 20(2), 223-238. https://doi.org/10.1111/j.1747-5457.1997.tb00774.x

Lavier, L. L., & Manatschal, G. (2006). A mechanism to thin the continental lithosphere at magma-poor margins. Nature, 440, 324-328. https://doi.org/10.1038/nature04608

Levell, B., Argent, J., Doré, A. G., & Fraser, S. (2010). Passive margins: overview. Geological Society, London, Petroleum Geology Conference series, 7, 823-830. https://doi.org/10.1144/0070823

Luth, S., Willingshofer, E., Sokoutis, D., & Cloetingh, S. (2010). Analogue modelling of continental collision: Influence of plate coupling on mantle lithosphere subduction, crustal deformation and surface topography. Tectonophysics, 484, 87-102. https://doi.org/10.1016/j.tecto.2009.08.043

McClay, K. R. (1990). Extensional fault systems in sedimentary basins: a review of analogue model studies. Marine and Petroleum Geology, 7, 206-233. https://doi.org/10.1016/0264-8172(90)90001-W

McClay, K. R., & White, M. J. (1995). Analogue modelling of orthogonal and oblique rifting, Marine and Petroleum Geology, 12, 137-151. https://doi.org/10.1016/0264-8172(95)92835-K

McClay, K. R. (1996). Recent advances in analogue modelling: uses in section interpretation and validation. Geological Society, London, Special Publication, 99, 201-225. https://doi.org/10.1144/GSL.SP.1996.099.01.16

McKenzie, D. (1978). Some remarks on the development of sedimentary basins. Earth and planetary science letters, 40, 25-32. https://doi.org/10.1016/0012-821X(78)90071-7

Michon, L., & Merle, O. (2000). Crustal structures of the Rhinegraben and the Massif Central grabens: An experimental approach. Tectonics, 19(5), 896-904. https://doi.org/10.1029/2000TC900015

Michon, L., & Merle, O. (2003). Mode of lithospheric extension: Conceptual models from analogue modeling. Tectonics, 22(4), 1028. https://doi.org/10.1029/2002TC001435

Molnar, N. E., A. R. Cruden, & P. G. Betts (2017). Interactions between propagat- ing rotational rifts and linear rheological heterogeneities: Insights from three-dimensional laboratory experiments. Tectonics, 36, 420–443. https://doi.org/10.1002/2016TC004447

Molnar, N. E., A. R. Cruden, & P. G. Betts (2018). Unzipping continents and the birth of microcontinents. Geology, 46(5), 451-454. https://doi.org/10.1130/G40021.1

Mulugeta, G. (1988). Squeeze box in a centrifuge. Tectonophysics, 148, 323-335.

https://doi.org/10.1016/0040-1951(88)90139-4

Nagel, T. J., & Buck, R. W. (1994). Symmetric alternative to asymmetric rifting models. Geology, 32(11), 937-940. https://doi.org/10.1130/G20785.1

Naylor, M. A., Laroque, J. M., & Gauthier, B. D. M. (1994). Understanding extensional tectonics: insights from sandbox models. Geodynamic Evolution of Sedimentary Basin, International Symposium, Moscow, 69-83.

Nestola, Y., Storti, F., Bedogni, E., & Cavozzi, C. (2013). Shape evolution and finite deformation pattern in analog experiments of lithosphere necking. Geophysical Research Letters, 40, 5025-5057. https://doi.org/10.1002/grl.50978

Nestola, Y., Storti, F., & Cavozzi, C. (2015). Strain rate-dependent lithosphere rifting and necking architectures in analog experiments. Journal of Geophysical Research: Solid Earth, 120, 584-594. https://doi.org/10.1002/2014JB011623

Oliveira, M. E., Gomes, A. S., Rosas, F. M., Duarte, J. M., França, G. S., Alemeida, J. C., & Fuck, R. A. (2022). 2D numerical modelling of double graben nucleation during early continental rifting: the role of crustal rheology and inherited mechanical weaknesses. Tectonophysics. https://doi.org/10.1016/j.tecto.2022.229281

Rudolf, M., Boutelier, D., Rosenau, M., Schreurs, G., & Oncken, O. (2016). Rheological benchmark of silicone oils used for analog modeling of short- and long-term lithospheric deformation. Tectonophysics, 684, 12-22. http://dx.doi.org/10.1016/j.tecto.2015.11.028

Tron, B., & Brun, J.-P. (1991). Experiments on oblique rifting in brittle-ductile systems. Tectonophysics, 188, 71-84. https://doi.org/10.1016/0040-1951(91)90315-J

Panien, M., Buiter, S. J. H., Schreurs, G., & Pfiffber, O. A. (2006). Inversion of a symmetric basin: insights from a comparison between analogue and numerical experiments. Geological Society, London, Special Publicaitons, 253, 253-270. https://doi.org/10.1144/GSL.SP.2006.253.01.13

Péron-Pinvidic, G., & Manatschal, G. (2010). From microcontinents to extensional allochthons: witnesses of how continents rift and break apart? Petroleum Geoscience, 16, 189-197. https://doi.org/10.1144/1354-079309-903

Ramberg, H. (1981). Gravity, Deformation and the Earth's Crust. Academic Press, London, United Kingdom.

Saria, E., E. Calais, D. S. Stamps, D. Delvaux, & C. J. H. Hartnady (2014). Present-day kinematics of the East African Rift. Journal of Geophysical Research: Solid Earth, 119, 3584–3600, https://doi.org/10.1002/2013JB010901

Samsu, A., Cruden, A. R., Molnar, N. E., & Weinberg, R. F. (2021). Inheritance of penetrative basement anisotropies by extension-oblique faults: Insights from analogue experiments. *Tectonics*, *40*, e2020TC006596.

https://doi.org/10.1029/2020TC006596

Sassi, W., Colletta, B., Balé, P., & Paquereau, T. (1993). Modelling of structural complexity in sedimentary basins: the role of pre-existing faults in thrust tectonics. Tectonophysics, 226, 97-112. https://doi.org/10.1016/0040-1951(93)90113-X

Schmid, T. C., Schreurs, G., Adam, J. (2022a). Characteristics of continental rifting in rotational systems: New findings from spatiotemporal high resolution quantified crustal scale analogue models. Tectonophysics, 822, 229174. https://doi.org/10.1016/j.tecto.2021.229174

Schmid, T., Zwaan, F., Corbi, F., Funiciello, F., & Schreurs, G. (2022b). Rheology of glucose syrup from the Tectonic Modelling Lab (TecLab) of the University of Bern (CH). GFZ Data Publication. **GFZ DATA PUBLICATION → TEMPORARY DROPBOX LINK:** https://www.dropbox.com/sh/1xq28itw0u1er9a/AADT1gmSThcKaNe28QykVnpJa?dl=0

Schori, M., Zwaan, F., Schreurs, G., Mosar, J. (2021). Pre-existing Basement Faults Controlling Deformation in the Jura Mountains Fold-and-Thrust Belt: Insights from Analogue Models. Tectonophysics, 814, 228980. https://doi.org/10.1016/j.tecto.2021.228980

Schreurs, G., Hänni, R., Panien, M., & Vock, P. (2003). Analysis of analogue models by helical X-ray computed tomography. Geological Society, London, Special Publications, 215, 213-223. https://doi.org/10.1144/GSL.SP.2003.215

Schreurs, G., Buiter, S. J. H., Boutelier, D., Corti, G., Costa, E., Cruden, A. R., et al. (2006). Analogue benchmarks of shortening and extension experiments. Geological Society, London, Special Publications, 253, 1-27. https://doi.org/10.1144/GSL.SP.2006.253.01.01

Schreurs, G., Buiter, S. J. H., Boutelier, D., Burberry, C., Callot, J.-P., Cavozzi, C. et al. (2016). Benchmarking analogue models of brittle thrust wedges. Journal of Structural Geology, 92, 116-139. https://doi.org/10.1016/j.jsg.2016.03.005

Smith, N. J. P., Shepherd, T. J., Styles, M. T., & Williams, G. M. (2005). Hydrogen exploration: a review of global hydrogen accumulations and implications for prospective areas in NW Europe. Geological Society, London, Petroleum Geology Conference series, 6, 349-358. https://doi.org/10.1144/0060349

Sokoutis, D., & Willingshofer, E. (2011). Decoupling during continental collision and intra-plate deformation. Earth and Planetary Science Letters, 305, 435–444. https://doi.org/10.1016/j.epsl.2011.03.028

Sun, Z., Zhong, Z., Keep, M., Zhou, D., Cai, D., Li, X., Wu, S., & Jiang, J. (2009). 3D analogue modeling of the South China Sea: A discussion on breakup pattern. Journal of Asian Earth Sciences, 34, 544–556. https://doi.org/10.1016/j.jseaes.2008.09.002

Unternehr, P., Péron-Pinvidic, G., Manatschal, G., & Sutra, E. (2010). Hyper-extended crust in the South Atlantic: in search of a model. Petroleum Geoscience, 16, 207-215. https://doi.org/10.1144/1354-079309-904

Vendeville, B., Cobbold, P. R., Davy, P., Brun, J. P., & Choukroune, P. (1987). Physical models of extensional tectonics at various scales. Geological Society, London, Special Publications, 28, 95-107. https://doi.org/10.1144/GSL.SP.1987.028.01.08

Warsitzka, M., Ge, A., Schönebeck, J.-M., Pohlenz, A., & Kukowski, N. (2019). Ring-shear test data of foam glass beads used for analogue experiments in the Helmholtz Laboratory for Tectonic Modelling (HelTec) at the GFZ German Research Centre for Geosciences in Potsdam and the Institute of Geosciences, Friedrich Schiller University Jena. GFZ Data Services. https://doi.org/10.5880/GFZ.4.1.2019.002

Wernicke, B., (1985). Uniform-sense normal simple shear of the continental lithosphere. Canadian Journal of Earth Sciences, 22(1), 108-125. https://doi.org/10.1139/e85-009

Willingshofer, E., & Sokoutis, D. (2009). Decoupling along plate boundaries: Key variable controlling the mode of deformation and the geometry of collisional mountain belts. Geology, 37(1), 39-42. https://doi.org/10.1130/G25321A.1

Willingshofer, E., Sokoutis, D., Luth, S. W., Beekman, F., & Cloetingh, S. (2013). Subduction and deformation of the continental lithosphere in response to plate and crust-mantle coupling. Geology, 41(12), 1239-1242. https://doi.org/10.1130/G34815.1

Willingshofer, E., Sokoutis, D., Beekman, F., Schönebeck, J.-M., Warsitzka, M., & Rosenau, M. (2018). Ring shear test data of feldspar sand and quartz sand used in the Tectonic Laboratory (TecLab) at Utrecht University for experimental Earth Science applications. V. 1. GFZ Data Services. https://doi.org/10.5880/fidgeo.2018.072

Weijermars, R., & Schmeling, H. (1986). Scaling of Newtonian and non-Newtonian fluid dynamics without inertia for quantitative modelling of rock flow due to gravity (including the concept of rheological similarity). Physics of the Earth and Planetary Interiors, 43, 316-330.

Wilson, J.T. (1966). Did the Atlantic close and then re-open? Nature, 211, 676-681. https://doi.org/10.1038/211676a0

Wilson, R. W., Houseman, G. A., Buiter, S. J. H., McAffrey, K. J. W., & Doré, A. G. (2019). Fifty years of the Wilson Cycle concept in plate tectonics: an overview. Geological Society, London, Special Publications, 470, 1-17. https://doi.org/10.1144/SP470-2019-58

Zou, C., Zhai, G., Zhang, G., Wang, H., Zhang, G., Li, J., et al. (2015). Formation, distribution, potential and prediction of global conventional and unconventional hydrocarbon resources. Petroleum Exploration and Development, 42(1), 14-28. https://doi.org/10.1016/S1876-3804(15)60002-7

Zwaan, F. (2017) 4D laboratory experiments of oblique extension and scissor tectonics, structural inheritance and sedimentation: implications for rift evolution, rift propagation and rift segment interaction, (Doctoral dissertation). Retrieved from BORIS repository (https://boristheses.unibe.ch/824/). University of Bern, Switzerland.

Zwaan, F., Chenin, P., Erratt, D., Manatschal, G., & Schreurs, G. (2021a). Complex rift patterns, a result of interacting crustal and mantle weaknesses, or multiphase rifting? Insights from analogue models. Solid Earth, 12, 1473-1495.
https://doi.org/10.5194/se-12-1473-2021

Zwaan, F., Chenin, P., Erratt, D., Manatschal, G., & Schreurs, G. (2021b). Competition between 3D structural inheritance and kinematics during rifting: Insights from analogue models. Basin Research, 00, 1-31.
https://doi.org/10.1111/bre.12642

Zwaan, F., & Schreurs, G. (in press). Analogue modelling of continental rifting: an overview. In Peron-Pinvidic, G. (Ed.): Rifted Margins, ISTE-WILEY.
https://doi.org/10.51926/ISTE.5061.6
Preprint link (Researchgate): https://www.researchgate.net/publication/349536310

Zwaan, F., & Schreurs, G. (2022a). Digital image correlation (DIC) and X-Ray CT analyses of lithospheric-scale analogue models of continental rifting. GFZ Data Services.
GFZ DATA PUBLICATION → TEMPORARY DROPBOX LINK:
https://www.dropbox.com/sh/n58nxx3yucugfsh/AAD87R8SO6aFZFg8xPUoUGzma?dl=0

Zwaan, F., & Schreurs, G. (2022b). A novel method for analogue modelling of lithospheric-scale rifting, monitored via X-Ray CT-scanning methods, at the University of Bern Tectonic Modelling Lab (CH). GFZ Data Services.
GFZ DATA PUBLICATION → TEMPORARY DROPBOX LINK:
https://www.dropbox.com/sh/7q4lgaf0t5u97g6/AADbzxhKOmamWaXrWOFpoytsa?dl=0

Zwaan, F., Schreurs, G., & Adam, J. (2018). Effects of sedimentation on rift segment evolution and rift interaction in orthogonal and oblique extensional settings: Insights from analogue models analysed with 4D X-ray computed tomography and digital volume correlation techniques. Global and Planetary Change, 171, 110-133.
https://doi.org/10.1016/j.gloplacha.2017.11.002

Zwaan, F., Schreurs, G., & Buiter, S. J. H. (2019). A systematic comparison of experimental set-ups for modelling extensional tectonics. Solid Earth, 1010, 1063-1097.
https://doi.org/10.5194/se-10-1063-2019

Zwaan, F., Schreurs, G., Naliboff, J., & Buiter, S. J. H. (2016). Insights into the effects of oblique extension on continental rift interaction from 3D analogue and numerical models. Tectonophysics, 693, 239-260.
http://dx.doi.org/10.1016/j.tecto.2016.02.036

Zwaan, F., Schreurs, G., & Rosenau, M. (2020). Rift propagation in rotational versus orthogonal extension: Insights from 4D analogue models. Journal of Structural Geology, 135, 103946.
https://doi.org/10.1016/j.jsg.2019.103946

Zwaan, F., Schreurs, G., Rudolf, M., & Rosenau, M. (2022). Ring-shear test data of feldspar sand from the Tectonic Modelling Laboratory at the University of Bern (Switzerland). GFZ Data services.
GFZ DATA PUBLICATION → TEMPORARY DROPBOX LINK:
https://www.dropbox.com/sh/3terjiq3ne0l0ki/AAA8GBEGwZf9qtt9TvGaEuZ6a?dl=0